HIGH-THROUGHPUT SCREENING IDENTIFIES MICRORNAS THAT TARGET NOX2 AND IMPROVE FUNCTION FOLLOWING ACUTE MYOCARDIAL INFARCTION

A Dissertation
Presented to
The Academic Faculty

by

Junyu Yang

In Partial Fulfillment
of the Requirements for the Degree
Doctor of Science in the
Biomedical Engineering

Georgia Institute of Technology
Emory University
MAY 2017

HIGH-THROUGHPUT SCREENING IDENTIFIES MICRORNAS THAT TARGET NOX2 AND IMPROVE FUNCTION FOLLOWING ACUTE MYOCARDIAL INFARCTION

Approved by:

Dr. Michael E. Davis, Advisor
School of Biomedical Engineering
Georgia Institute of Technology

Dr. Haifeng Chen
School of Biomedical Engineering
Peking University

Dr. Jianzhong Xi, Advisor
School of Biomedical Engineering
Peking University

Dr. Yangming Wang
School of Biology Science
Peking University

Dr. Changhui Li
School of Biomedical Engineering
Peking University

Dr. Junbiao Dai
School of Biology Science
Tsinghua University

Date Approved: 03 28, 2017

ACKNOWLEDGEMENTS

This dissertation would not have been finished without the help of numerous people. I owe my gratitude to all these people.

First, I would like to express my gratitude to Dr. Jianzhong Xi, my advisor in Peking University. Your continuous instruction and encouragement make it possible for me to move to this step. When I entered the Ph.D. program, I never expected to have an academic career in the future. Your patience, understanding, and passion for science encourage me to achieve more in scientific research.

Next, I would like to thank my advisor in Georgia Institute of Technology, Michael E. Davis. Although it was only one year to stay in your lab, it would be the most memorable experience in my life. You are an awesome advisor, making me feel so comfortable to stay in another country.

I also would like to thank my these committee members, Dr. Huaiqiu Zhu, Dr. Haifeng Chen, Dr. Yangming Wang, Dr. Junbiao Dai, and Dr. Qiong Wu for their precious time and valuable suggestions for the work done in this dissertation.

Next, I would also like to thank my fellow lab members who provided great collaboration and assistance during my study. You have made my research life much more successful.

Finally, my special appreciations go out to my family to whom I owe so much. Your support and encouragement give me the power to aim higher in everything I do.

TABLE OF CONTENTS

LIST OF TABLES

LIST OF FIGURES

LIST OF SYMBOLS AND ABBREVIATIONS

SAMCell	self-assembled cell microarray
miRNA	microRNA
ECM	extracellular matrix
RNAi	RNA interference
mRNA	messenger RNA
siRNA	small interfering RNA
pri-miRNA	primary microRNA
pre-miRNA	precursor microRNA
RISC	RNA induced silencing complex
UTR	untranslated regions
HTS	high-throughput screening
eGFP	enhanced green fluorescent protein
PNI	Poly (N-isopropylacrylamide)
PR	positive representative
NR	negative representative
FC	fold change

NC	negative control
No.	number
HF	heart failure
MI	myocardial infaction
GO	gene ontology
PPIs	protein-protein interactions
DND	detonation nanodiamonds
Dox	doxorubicin
PLT	platelet count
RDW-CV	red blood cell distribution width
RBC	red blood cell counts
HCT	hematocrit
MCV	mean corpuscular volume
MHC	hemoglobin
MCHC	mean corpuscular hemoglobin concentration
WBC	white blood cell counts
NEU	neutrophil counts

LYM	lymphocyte counts
uGLU	urine glucose
uPRO	urine protein levels
uLEU	urine leukocytes
uERY	urine erythrocytes

SUMMARY

MicroRNAs (miRNAs) are small non-coding RNAs that can regulate gene expression by inducing either degradation or translational inhibition of a target mRNA. miRNAs have been indicated to regulate up to 90% of human genes and played significant role in heart diseases.

Myocardial infarction (MI) is the most common cause of heart failure. Excessive production of reactive oxygen species (ROS) plays a key role in the pathogenesis of cardiac remodeling after MI. NADPH with Nox2 as the catalytic subunit is a major source for cardiac superoxide production. Nox2 expression is significantly increased in the infarcted area, especially in macrophages and myocytes. Mice lacking the Nox2 gene are protected from heart injury.

Here we demonstrate to utilize the screening of the miRNA-targets using self-assembled cell (SAMcell) microarray to identify miRNAs that could regulate Nox2 expression and select three miRNAs, miR-106b, miR-148b, and miR-204, for further study. We use different in vitro assays to validate these miRNAs function on Nox2 expression and downstream products. After that we use acid-degradable polyketal particles that could effectively encapsulate miRNAs and deliver them into macrophages. Both in vitro and in vivo studies confirmed the PK3-miRNAs particles could inhibit Nox2 expression and activity, and significantly improve cardiac function. These results revealed new miRNAs for heart disease treatment and provided an effective strategy from miRNAs identify to in vivo delivery.

Our study successfully combine the miRNAs high throughput screening system and macrophages specific delivery system and establish an easy and efficient method from screening

to drug delivery. We validate this system and the selected miRNAs functions both in vitro and in vivo. This provides us new evidence and directions for not only myocardial infarction recovery, but also other inflammation related diseases.

CHAPTER 1. INTRODUCTION

1.1 The Significance of Cardiovascular Disease and Research:

Currently in the world, cardiovascular disease (CVD) is the major cause of death. Of those CVD related mortalities, deaths from heart attacks, which also be known as myocardial infarction (MI), contribute to the largest percentage. In 2013, more than half million Americans had a heart attack for the first time, while half of those had a recurrent attack; another 150,000 silent attacks went undiscovered, that means totaling about one attack every thirty-four seconds, while approximately one people would die because of a heart attack every minute[1].

Despite these appalling statistics, progresses in patient healthcare have raised the possibility to survive after an acute MI. However, structural responses of the heart during wound healing may lead to progressive heart failure. Cardiac remodeling, the host of structural changes, offers a new window of therapy. It aims at limiting these adverse remodeling events and improving patient outcomes of therapy. Therefore, extensive research

into the pivotal events and mediators of the cardiac remodeling process is in highly demand to exploit and improve current therapies.

1.2 Ischemic Injury After Myocardial Infarction

Myocardial infarction is a kind of ischemic disease. It's usually followed by plaque or thrombus formation inside a coronary vessel. Consequently, the blood flow to the downstream myocardium will be disrupted[2] (Figure 1-1). The term "ischemia" means to "restrain blood" or "without blood." Nowadays, investigators specifically define ischemia in the heart as an insufficient in the supplement of substrates and oxygen to meet the requirements in order to maintain normal function of myocardium[2][4][5]. Ischemia is different from "hypoxia". There is a accumulation of metabolic wastes in ischemic area as a result of the limited blood flow, which does not happen during hypoxia. This will excessively contributes to ischemic damage[5]. Following MI, the shortage supplement of oxygenated blood to the ischemic area results in a fast decreases in oxygen level that available to the myocardium. This will reduce the oxidative phosphorylation rate by the

mitochondria of cardiac myocytes and consequently, ATP production. In order to preserve function, cardiac myocytes, which are essential contractile cell for the heart, depend mostly on a less efficient, but normal, anaerobic glycolysis to generate ATP. However, contractile disorders are unavoidable. Because the consumption of ATP stores will result in failure of Na^+/K^- ATPases, disturbed Ca^{2+} handling and eventually the loss of the homeostatic intracellular environment. Areas of reversible myocytes dysfunction will transit into a zone of irreversible ischemic damage without the restoration of oxygenated blood flow. This area is defined as the "infarct zone," marked with cell death by necrosis, apoptosis and autophagy[6]. After this, infarct scar is developed to stabilize the necrotic region and prevent ventricular rupture, as the result of activation of the cardiac wound healing process. In severe cases of MI, maladaptive cardiac remodeling responses that keep the heart in a state of chronic dysfunction is caused by extensive myocytes loss.

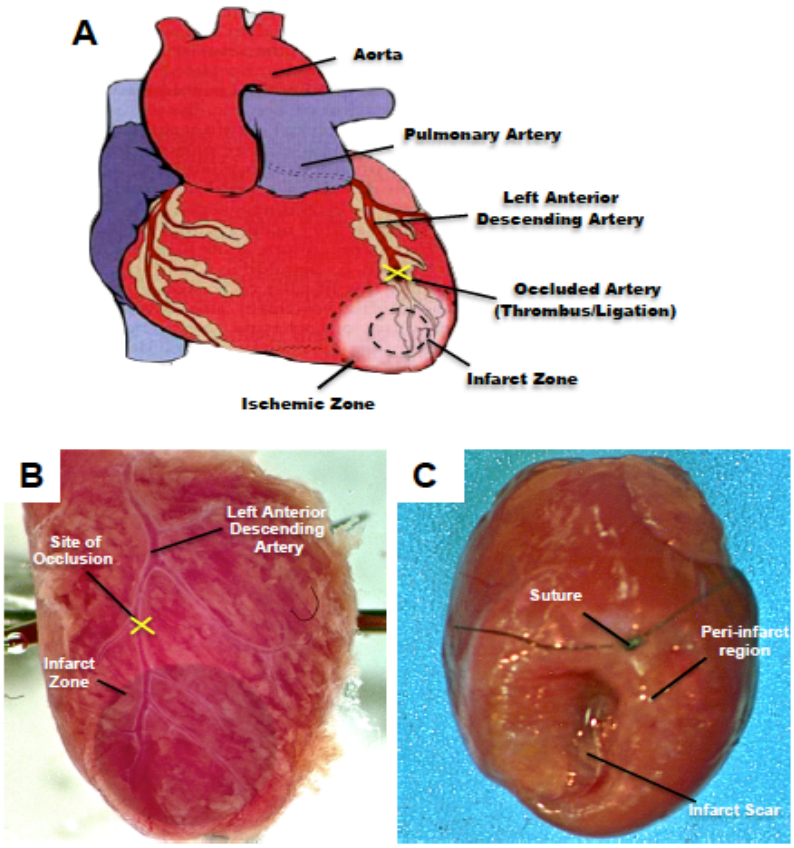

Figure 1-1: Schematic diagram of myocardial infarction. A, Occlusion of the left anterior descending artery (LAD) leads to a shortage supply of blood and substrates to the downstream myocardium known as myocardial "ischemia". B, A mouse model of MI injury and repair has been developed which utilizes surgical ligation of the LAD artery to trigger a wave of necrosis in the downstream myocardium, refers to the infarct zone, leading to the formation of a infarct scar C, on the antero-apical wall of the left ventricle.

Besides of the challenging techniques needed to induce MI, the progression and prognosis of post-MI remodeling is a complex disease to research because of a range of stimuli from different sources. Despite of this fact, a MI model has still been generated in different species including the monkey, pig, dog, cat, rabbit, rat, and mouse[10-13].

Canonically, animal models of MI are produced via surgical induction of coronary artery occlusion. This is most commonly done with the left anterior descending (LAD) artery to block the flow of blood to the anterior wall and apex of the left ventricle (LV) (Figure 1-1).

1.3 Inflammation

Hearts are unable to regenerate functional myocytes, which might be the major complication to treat an MI. This also makes it incapable for hearts to be fully recovered from irreversible ischemic damage and vulnerable to heart failure. Consequently, the process becomes unavoidable that wound healing is quickly initiated to take place and enforce the ischemic regions via developing an infarct scar. During this process, cells from the inflammatory system work together with wound healing cells through chemical modulators, such as cytokines, inducing the activation and orchestration of the wound repairing process.

Following MI, he transcription factor Nuclear Factor (NF) in resident cells will be activated by the necrosis in the infarcted region. This also triggers the production of chemokines (i.e. Monocyte Chemoattractant Protein (MCP)-1), cytokines (i.e. Tumor

Necrosis Factor (TNF), interleukin), and adhesion molecules[14-16]. These chemokines and cytokines induce related signaling pathways and establish a "pro-inflammatory" environment, marked by extensive degradation of extracellular matrix (ECM) via activation of matrix metalloproteases (MMPs), which are secreted by cardiac fibroblasts (CFs). There are also other kind of cells that targeted to the injury site, including the pro-inflammatory M1 macrophages, mast cells, neutrophils, and lymphocytes. These cells will begin to clear of cellular debris in the infarcted area. Once finished, apoptosis of these recruited neutrophils activate expression of IL-10 and transforming growth factor (TGF) from macrophages. Consequently, the inflammatory processes will be repressed[17-18].

These inflammatory chemokines also initiate the proliferation of cardiac fibroblast and endothelial cell proliferation[17, 19]. During this process, cytokines such as TGF-β stimulate the transition from the pro-inflammatory M1 macrophage to the M2 macrophage. This wound healing process helps in repair following MI and express enzymes important for ECM remodeling[18]. Moreover, TGF-β and other hormones, which commonly expressed in the tissue after MI such as angiotensin II (Ang II), also induce cardiac fibroblast

differentiation and activation into myofibroblasts. This kind of cells secrete large amounts of collagen, mostly type I and type III, to preserve the infarcted area structural integrity and prevent ventricular rupture. This is fulfilled by form a new microvascular network via endothelial cells[20-21]. Following wound stabilization, a mature, densely arranged collagenous infarct scar is formed by fibroblasts apoptosis and inflammatory process maturation[16].

1.4 Cardiac Remodelling

The cardiac remodeling is described as the geometrical changes happening in the LV of post-MI hearts, more specifically referring to dilation of the LV cavity[22]. Up to now, large amounts of studies have expanded the principle of cardiac remodeling. Now it is defined as a variety of clinical scenarios resulting into downstream different paths of pathological remodeling. However, all of these converge on one common outcome, ventricular dysfunction[23].

The cardiac remodeling process post-MI is more complex compared to other CVDs. Because there are various types of inflammatory imposed to the myocardium, as well as biomechanical stress. These are not happened in other disease. The post-MI remodeling process is so complex that includes responses for infarct expansion, pressure overload, and subsequent raise in wall-stress. However, these responses eventually push the patient into serious dilated heart failure (Figure 1-2)[23-24]. Early compensatory cardiac hypertrophy, wall thinning and LV chamber dilation, infarct expansion, and tissue fibrosis are resulted from heart failure related geometrical changes. All of these could be visualized and quantified by in vivo imaging techniques such as echocardiography[25]. Typically, parameters, like interstitial collagen, volume of LV end-diastolic, area of myocyte cross-sectional, can be used as good indicators of pathological cardiac remodeling[26-29].

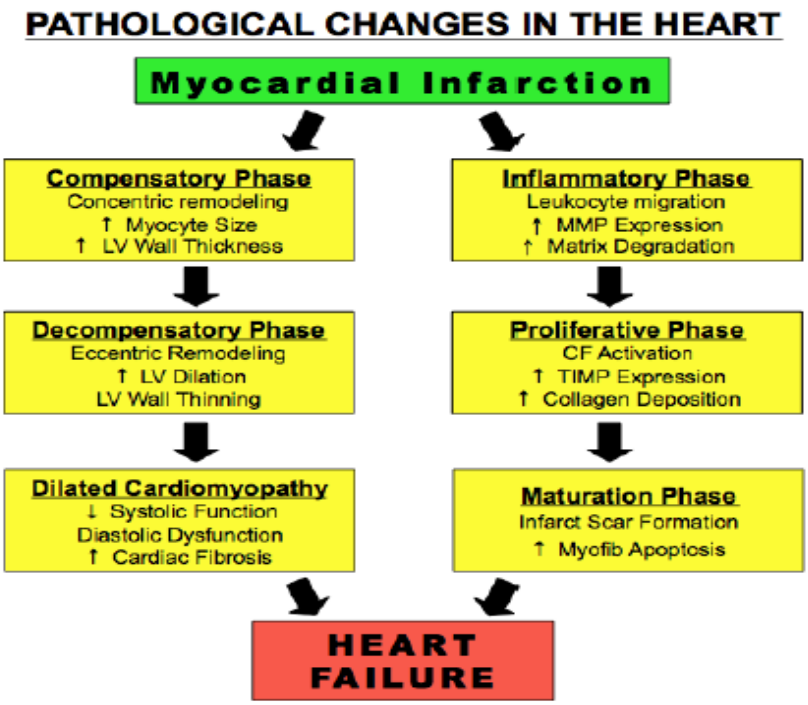

Figure 1-2: Model of pathological responses by the heart to MI injury. Following severe cases of MI, a series of temporal wound healing responses at the molecular, cellular and tissue level occur, leading to adverse cardiac remodeling events and results in dilated cardiomyopathy, cardiac fibrosis and eventual heart failure.

Following MI, it's in a higher functional demand on the remaining viable, non-infarcted myocardium to maintain enough cardiac function, due to heart myocytes lost in the infarcted areas. Hypertrophy is a compensatory response activated related to this increased mechanical demand. This will result into an increase in the amount of contractile units (sarcomeres) per cardiac myocyte and thickness of myocardial wall. These changes help heart to maintain cardiac function and normalize wall-stress (Law of Laplace), respectively[23-24]. Besides of

these physical factors, other various types of stimulations, including the hormones, growth factors such as insulin-like growth factor-1 (IGF-1), fibroblast growth factor (FGF) and cytokines like TGF-β also contribute to cardiac myocyte hypertrophy. These stimulations are frequently presented in the post-MI heart, activating different kinds of signaling pathways within myocytes. Cardiac myocyte hypertrophy is marked by increased volume and number of cells, enhanced protein expression, which is consistent with the gene expression profile in the developing fetal heart[30].

Eventually, because of the fact that increased expression and synthesis of contractile proteins cannot be maintained, the compensatory hypertrophy in non-infarcted areas reduces. The remaining viable myocardium sustains reduced contractility. This leads to a decline in cardiac function and subsequent LV volume overload. As LV end-diastolic volume and pressure raises, LV wall thins because myocytes are forced to stretch and expand the infarcted regions. Meanwhile, these can further increase LV chamber dilation and wall stress. Other factors, such as apoptosis, myocytes rupture, decline in the intercellular space, also contributing to wall-thinning and infarct area expansion[24]. In previous post-MI studies

performed on mice, an increase in LV end-diastolic volume and wall-thinning outside of infarcted areas had been demonstrated as early as 18 days after coronary artery ligation[28, 31]. During this time point, the heart is in an irreversible progression towards heart failure. Meanwhile, continued biomechanical and chemical stress, serving as a chronic inducer of cardiac fibroblasts in the myocardium, worsens the prognosis. Therefore, this constant stimulation leads to over-production and deposition of ECM by cardiac fibroblasts. Consequently, cardiac fibrosis is initiated and infiltrated into the un-infarcted areas, making the myocardium stiffer, and further damage cardiac function[32].

1.5 ROS and Nox2 in MI

While studies show that low levels of reactive oxygen species (ROS) are physiologically important, production of excessive amounts of ROS is a key event involved in post-MI pathogenesis4. ROS modulate several processes during cardiac remodeling, including interstitial fibrosis, and cardiomyocyte apoptosis and hypertrophy[33-34].

Many studies demonstrate that a major source for ROS in the heart comes from a family of nicotinamide adenine dinucleotide phosphate- (NADPH) oxidase enzymes[35]. NADPH oxidase is a multi-subunit enzyme consisting of membrane proteins (gp91phox otherwise known as Nox and p22phox) and several intracellular associated proteins (p47phox, p67phox, Rac). Five Nox isoforms (Nox1 to Nox5) exist and are thought to the major indispensable subunit. Among these, Nox2 is expressed in cardiomyocytes, fibroblasts, and endothelial cells, and is thought to be dominant Nox isoform contributing to cardiac superoxide levels (O_2^-) production[33, 36]. Evidence shows that both in animal models of MI and patients with end-stage heart failure, Nox2 expression is significantly increased in the infarcted myocardium, primarily in macrophages and myocytes[37-38]. Nox2 knockout mice show reduced cardiomyocyte apoptosis and adverse remodeling after MI and attenuate interstitial fibrosis following aortic constriction[39]. In addition, as there is no specific inhibitor of Nox2, studies from our own laboratory have shown that Nox2 siRNA delivered in polymeric nanoparticles can attenuate acute cardiac dysfunction following MI as a potential therapeutic alternative[40].

1.6 miRNA

MicroRNAs are a kind of small, non-coding ribonucleic acids (RNAs). They were first discovered as elements essential for development of Caenorhabditis elegans (C.elegans)[41-44]. Lin-4 was the first reported small non-coding RNA, which was essential for larval development of C.elegans. This small RNA was then demonstrated to be able to suppress a target protein via RNA::RNA sequence complementary binding within the messenger RNA (mRNA) 3'untranslated region (3'UTR) of the target[41, 43, 44]. Let-7, another key small RNA involved in regulation of C.elegans development, was then discovered. Since let-7 is highly conserved among species, this discovery paved the way for this regulatory mechanism to be expanded to multiple specie[43, 45]. In 2001, for the first time, researchers cloned the first set of these small RNAs (33 in total) from a human cell line, and coined them as the term microRNA[46-48]. After these studies, there are more than one thousand of miRNAs have been discovered within the human genome and they are predicted to target more than one third of human genes[49].

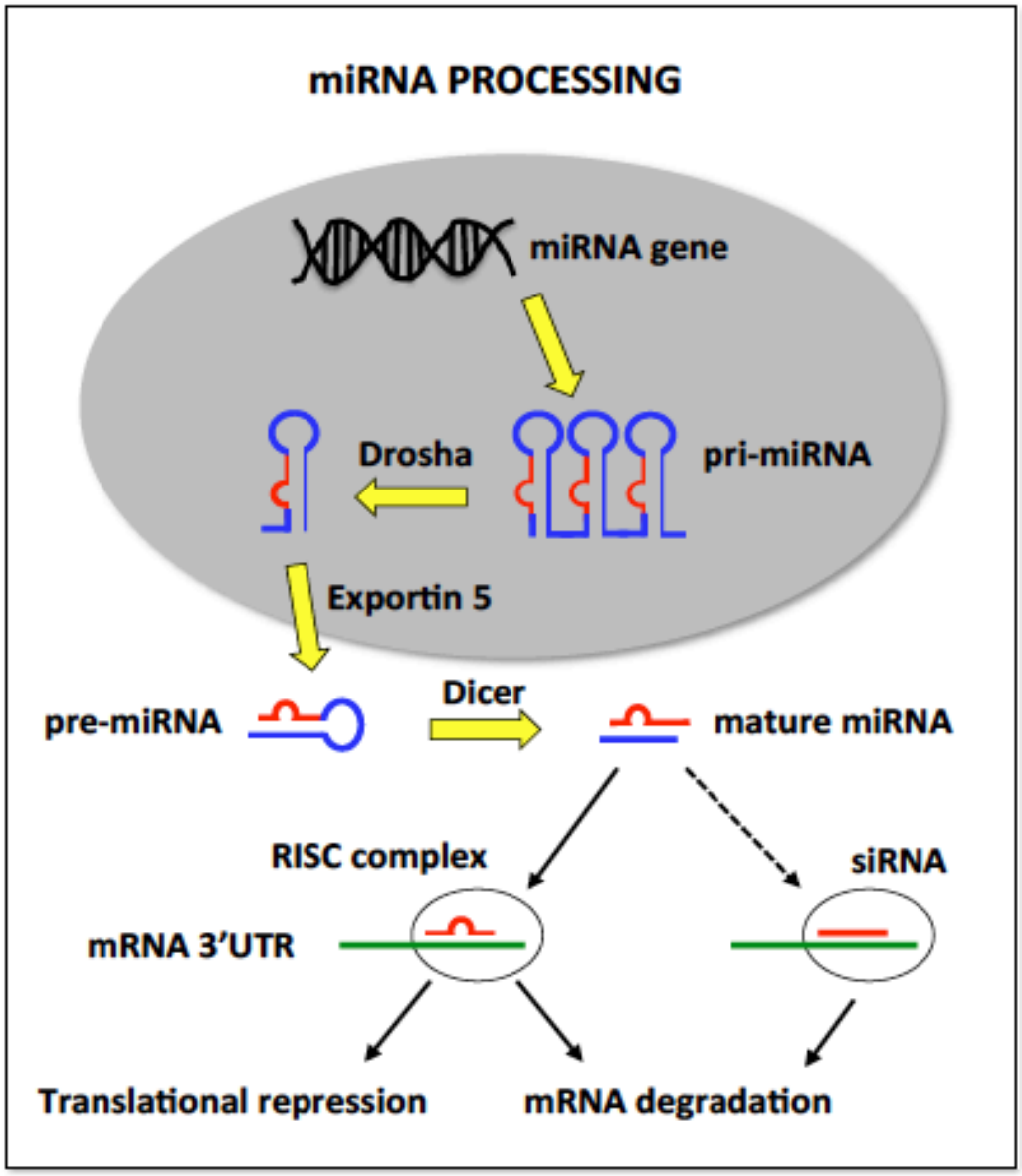

Figure adapted from He, L. et al., Nature Reviews, 2007.

Figure 1-3: Schematic of microRNA processing. MicroRNAs are transcribed in the nucleus by polII which produces a pri-miRNA transcript. This transcript is then processed by Drosha into a pre-miRNA sequence, and exported out of the nucleus by Exportin5. Dicer then further processes the pre-miRNA into the double stranded mature miRNA sequence. Mature miRNA product is incorporated into the RISC complex, and after degradation of the anti-sense strand, the miRNA binds to the 3'UTR

of target mRNA based off complementary sequence. Target expression is repressed either by mechanisms of translation inhibition or mRNA degradation.

MicroRNAs can locate inter- or intragenic. They are usually transcribed as distinct pri-miRNA transcripts via polymerase II (Figure 1-3)[49-50]. MicroRNAs can be transcribed both as single miRNA hairpins and as polycistronic clusters. After transcription, the pri-miRNA is processed through an RNase III enzyme Drosha into a 60-90 nucleotide (nt) pre-miRNA construct. Then Exportin5 export this pre-miRNA out of the nucleus. The pre-miRNA is then further processed into the double stranded mature miRNA sequence within the cytoplasm. Then the RNA-induced silencing complex (RISC) incorporates this 20-25nt long double-stranded RNA and the mature sequence is released by preferential degradation of the antisense strand. The RISC complex is the functional unit of the miRNA machinery. This complex will bind to the 3'UTR of the target mRNA based on sequence complementarity[49-50]. Unlike small interfering RNA (siRNA) the binding of miRNA to mRNA has a degree of imperfect complementary. This leads to a different method of functional suppression, including both mRNA degradation and translational inhibition[49]. The precise mechanisms of repression are still not quite clear but mRNA degradation seems to happen through

deadenylation and recruitment to processing bodies, while translational inhibition usually can occur at the level of initiation or elongation[51].

Several clues pointed to a participation of miRNAs in cardiac disease. In failing hearts, a profibrotic role was attributed for miR-21[52]. Therapeutic miR-21 antagonism was shown to reduce progression of maladaptive fibrosis. Contrary to standard pharmacological agents targeting only single molecular pathways, miRs are capable of regulating multiple downstream mediators in parallel, thus affecting various signaling cascades. Van Rooij et al[53] nicely demonstrated the direct impact of miR-29 expression for fibrotic scar formation in the failing heart. Next to the development of cardiac fibrosis, miR-133 was closely linked to cardiomyocyte function by altering hypertrophic response[54]. MiRs were also shown as therapeutic entry points in several MI-related disease settings (eg, miR-92a, miR-24)[55-56], and its use as biomarkers for heart disease has recently been discovered intensively[57-59].

1.7 High-throughput miRNA-targets screening system

The critical challenge in miRNA therapy for cardiac disease includes identifying miRNAs that can target important genes and delivering them into specific cells efficiently. A certain miRNA normally has hundreds of targets, which is difficult to validate only by database prediction. Most published works using high-throughput miRNA target validation are used to identify targets of a miRNA[60-62]. But for a specific pathological disease, in which we already know which genes play important roles, it is more useful to find and select miRNAs that can target those genes directly. As Nox2 has no specific inhibitor and plays such an important role in post-MI pathogenesis, finding new ways to reduce expression could generate new therapeutic options. Moreover, to date, there have been no reports of miRNAs that target Nox2 directly and reduce expression. In this study, we demonstrate use of a self-assembled cell microarray (SAMcell) to find miRNAs that target Nox2 and deliver them into myocardial macrophages via acid-degradable polymers previously shown to deliver siRNA in to macrophages[40]. The SAMcell system had been demonstrated for its efficient and accurate miRNA targeting identification by our previous work[63]. SAMcell

assays using the 3'UTR of Nox2 identified many potential miRNAs that were then tested in reporter cells, as well as mouse and human macrophages.

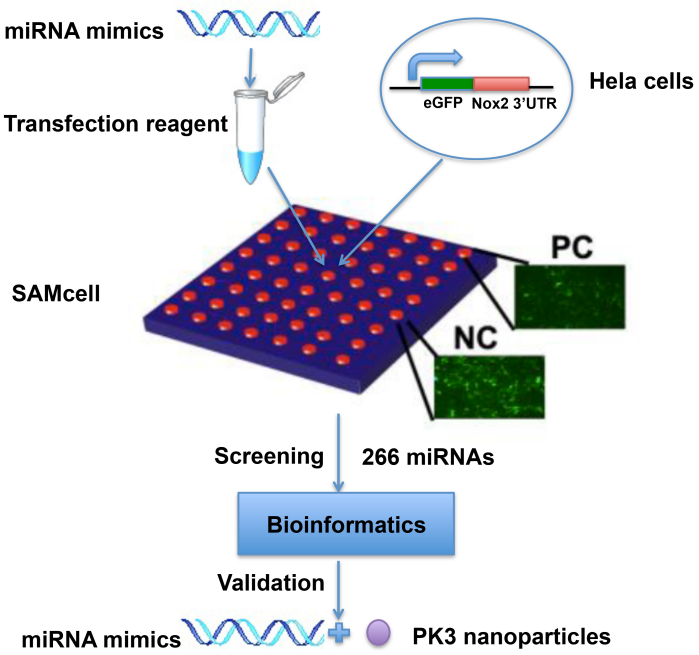

Figure 1-4: Schematic diagram of the screening strategy to identify miRNAs targeting human Nox2. miRNA mimics were printed on the self-assembled cell microarray together with the transfection reagent. Hela cells stably expressing enhanced green fluorescent protein (eGFP) fused with the 3'UTR from human Nox2 were seeded on the array. Human Nox2 siRNA was used as positive control (PC) and scrambled miRNA was used as negative control (NC). In total, 266 miRNAs with conserved sequences between humans and mice were screened. After bioinformatics analysis and validation, three miRNAs were chosen for further study.

1.8 Polyketal PK3 Nanoparticles.

Polyketals (PKs) are a class of delivery vehicles formulated from a class of polymers that contain pH sensitive, hydrolyzable ketal linkages in their backbone. Unlike the predominantly polyester based delivery vehicles currently of use, PKs do not generate acidic degradation products as they degrade into acetone and diols[64]. The polymerization strategy is such that it is possible to form polymers between any diol and 2,2-dimethoxypropane affording great flexibility for generating biomaterials with properties such as variable hydrolysis and pH sensitivities suitable for a variety of applications[65, 68]. The properties of PKs can be easily modified to alter particle size, shape and porosity. Among these, the polyketal copolymer PK3 formed by reacting the diols cyclohexanedimethanol and 1,5-pentanediol with 2,2-diethoxypropane makes an excellent delivery vehicle for siRNA due to its faster hydrolysis at the acidic pH of the endosome. In a previous study where PK3 was used to deliver TNF-α siRNA to liver macrophages in vivo, a hydrolysis half-life of 1.8 days at pH 4.5 and 39 days at pH 7.4 was reported[69]. Additionally, PK3 is a hard material that is water insoluble and can maintain its integrity in vivo due to the high energy cost of being exposed to water, providing serum stability[68-69]. Published studies from our laboratory

demonstrate that polyketal nanoparticles are retained in the myocardium following injection and are stable at neutral pH levels[66, 68]. When engaged by macrophages, present in high quantities during MI, particles are taken up and trafficked into phagosomes/endosomes where they degrade due to the acidic environment. Although the mechanism of release of siRNA is not clearly known, it is speculated that after phagocytosis/endosomes, these particles hydrolyze and potentially cause an osmotic imbalance within these compartments, leading to release of siRNA into the cytoplasm in a timely manner.

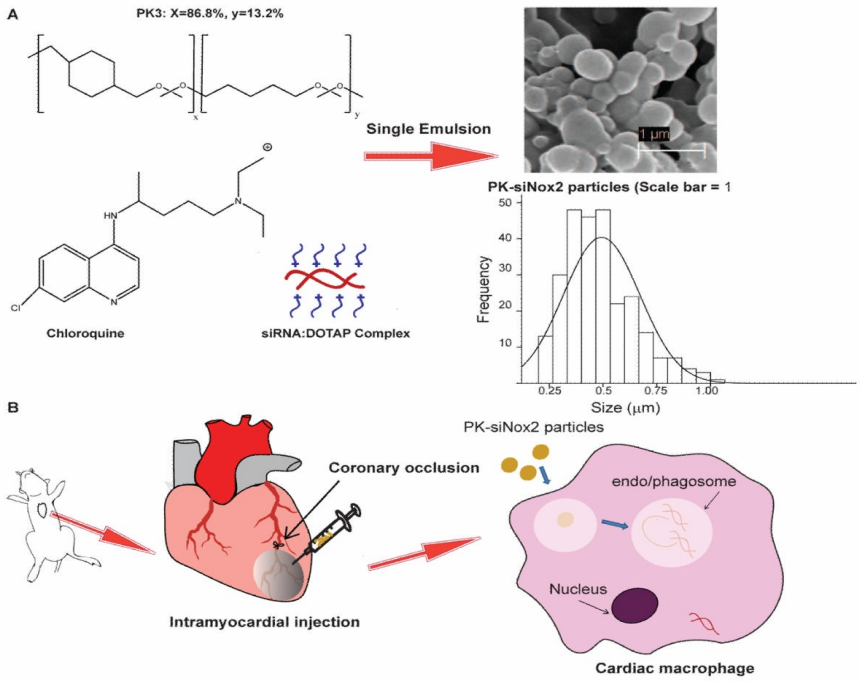

Figure 1-5: Schematic of PK-siNox2 particle formulation and delivery. (A) Ion-paired siRNA:DOTAP and endosomal disruptive agent chloroquine are encapsulated into the PK3s via a single emulsion/solvent evaporation procedure generating submicron

particles (500 ± 175 nm). (B) The PK3s encapsulating siRNA are intramuscularly injected into mice hearts following permanent coronary occlusion (MI) surgery. The particles are taken up my macrophages in vivo with high efficiency due to their ability to protect siRNA from serum proteins and stimulate phagocytosis and/or endocytosis. Once taken up, they degrade in the acidic environment within these compartments due to the acid- sensitive ketal linkages in PK3 (also aided by chloroquine) and escape the phagosome/ endosome via a colloid osmotic mechanism to release siRNA into the cytoplasm.

CHAPTER 2. SAMCELL SCREENING TO TARGET HUMAN NOX2

2.1 Fabrication of SAMCell

Glass slides (2.2 cm×2.2 cm) were washed with detergent and miliQ water. After dryness, the slides were covered with poly (N-isopropylacryla-mide) (Aldrich) dissolved in ethanol (6% (w/v). The slides were etched via a shadow mask by oxygen plasma for 3.5 min at 200 W. The reverse transfection protocol refers to previous description32. In brief, 3 μl of OptiMEM (Invitrogen), containing sucrose and Lipofectamine 2000 (Invitrogen) were transferred to each tube and mixed thor- oughly. Then, 1 μl siRNA (100 μM) was added to each tube and the mixture was incu- bated for 20 min at room temperature. Finally, 7.25 μl of a 0.2% (w/v) gelatin (Sigma, Type B) solution was added to each tube and mixed thoroughly. After ultraviolet sterilization, the reverse transfection reagent was printed either on the chip via a nanolitre microfluidic dispenser we recently created33, or on a commercially available nanodispenser (Phoenix, Art Robbins Instruments). Next, the slides were fixed in a six-well plate by melted wax. About 3 ml 37 °C medium containing 5×105 cells were transferred in each well. About 24–48 h later, the dishes were moved at room tem-

perature for 5 min and washed with PBS for three times to ensure the total removal of the polymer. Then the cell microarray was recorded by a microscope system.

2.2 Construction of Report System

The 3'UTR of human Nox2 gene was cloned by PCR and linked to the end to eGFP protein. To establish stable cell lines, the lentiviral vector containing eGFP and human Nox2 3'UTR was packaged in 293T cells. After 72 h, eGFP-positive cells were collected by FACS. Alternatively, 48 hours after infection, medium was changed, and puromycin (Sigma) was added to the medium and the selection was carried out for 3-5 weeks.

2.3 miRNA-targets screening

Over 260 miRNAs were printed on SAMcell microarrays. Then, 5×10^5 cells containing 3'UTR reporter were transferred in each well. About 24-48 h later, the dishes were moved at room temperature for 5 min and washed with PBS for three times to ensure the total removal of the polymer. Average fluorescent intensity of each cell island were

collected and analyzed. The cut-off value was obtained on the basis of the Kolmogorov-Smirnov Z-test in 50 control experiments. For each miRNA, at least 6 times were repeated.

2.4 Screening results

The top effective miRNAs are listed in Table 1. Three miRNAs, miR-106, miR-148b, and miR-204 were selected for further study after literature research and miRNA target prediction. Each of them have one or more predicted binding sites in human Nox2 3'UTR according to Targetscan database, shown in Table 2.

Table 1: Top listed results of SAMCell

miRNA	Fold Change	P-value
miR-106b	0.9000	0.0003
miR-148b	0.9010	0.0001

Table 1 continued		
miR-21	0.9049	0.0191
miR-135b	0.9150	0.0004
miR-296-5p	0.9155	0.0005
miR-590-5p	0.9209	0.1019
miR-33a	0.9233	0.0289
let-7f-1-3p	0.9250	0.0498
miR-29c*	0.9258	0.0037
let-7i	0.9265	0.0268
miR-204	0.9278	0.0082
miR-221	0.9315	0.1212
miR-190	0.9337	0.1169

Table 1 continued		
miR-7	0.9355	0.0581
miR-331-3p	0.9362	0.0463

Table 2: miRNAs-Nox2 predicting binding sites from Targetscan database

	Predicted consequential pairing of target region (top) and miRNA (bottom)
Nox2 3'UTR Has-miR-106b	5' ...UCUAUGGUUUUGAGAGCACUUUU... |||||| 3' UAGACGUGACAGUCGUGAAAU
Nox2 3'UTR Has-miR-148b	5' ...CCCAGAAUCCUCAGGGCACUGAG... |||||| 3' UGUUUCAAGACAUCACGUGACU

Table 2 continued	
Nox2 3'UTR	5' ...UCAAUUUUAGAAUCAAAAGGGAA...
	|||||||
Has-miR-204	3' UCCGUAUCCUACUGUUUCCCUU
Nox2 3'UTR	5' ...AAAAUAAAAAAGGCAAAAGGGAG...
	||||||
Has-miR-204	3' UCCGUAUCCUACUGUUUCCCUU

CHAPTER 3. SELECTED MIRNAS FUNCTIONAL VALIDATION

3.1 Cell Culture

293T and Hela cells were cultured in high-glucose Dulbecco's Modified Eagle Medium (DMEM) containing 10% fetal bovine serum (FBS), 100 units/ml penicillin and 0.1 mg/ml streptomycin (P/S). RAW 264.7 and THP-1 cells were cultured RPMI 1640 containing same amounts of FBS and P/S as above. All cells were cultured under humidified conditions in 5% CO_2 at 37°C. When seeding, cells were washed with PBS and incubated in 0.25% trypsin containing 5mmol/L EDTA. After centrifugation, cells were diluted in media, counted via hemocytometer, and then seeded at the appropriate concentration.

3.2 miRNA Transfection

miRNA mimics were obtained from GenePharma and Sigma. To achieve transient expression, plasmids and miRNA mimics were transfected using Oligofectamine (Invitrogen) following the protocol below:

1. One day before transfection, plate cells in 100 µL of growth medium without antibiotics so that cells will be 30–50% confluent at the time of transfection.

2. For each transfection sample, prepare complexes as follows:

a. Dilute 1 µL of a 20 µM stock oligonucleotide in 16 µL of Opti-MEM I Reduced Serum Medium without serum to a final volume of 17 µL. Mix gently.

b. Mix Oligofectamine Reagent gently before use, then dilute 0.4–0.8 µL in Opti-MEM I Mediumwithout serum to a final volume of 3 µL. Mix gently and incubate for 5–10 minutes at room temperature.

c. Combine the diluted oligonucleotide with diluted Oligofectamine Reagent (total volume = 20 µL). Mix gently and incubate for 15–20 minutes at room temperature (the solution may appear cloudy).

3. While complexes are forming, remove the growth medium from the cells and wash once with medium without serum. Add 80 µL of medium without serum to each well containing cells.

4. Mix the 20 μL of complexes (from step 2c of this procedure) gently, and add to the cells.

5. Incubate the cells at 37°C in a CO_2 incubator for 4 hours.

6. Add 50 μL of growth medium containing 3X the normal concentration of serum without removing the transfection mixture.

3.3 Luciferase Assay

The 3'UTR of human or mouse Nox2 were cloned into pGL3 plasmids 3'UTR to the firefly luciferase gene. Four x 10^4 293T cells were co-transfected with 200 ng of the indicated pGL3 firefly luciferase construct and 20 ng of a pGL3 Renilla luciferase used as a normalization control. At the same time, the indicated miRNA expression plasmid or mimics were transfected. After 48 hours, cells were lysed and luciferase activities were measured using the Dual Luciferase Reporter Assay System (Promega).

3.4 RNA Isolation

Total RNA from cells was isolated using Trizol (Invitrogen) according to the manufacturer's protocol. Briefly speaking, rinse cell monolayer with ice cold PBS once. Lyse cells directly in a culture dish by adding 1 ml of TRIZOL Reagent per 3.5 cm diameter dish and scraping with cell scraper. Pass the cell lysate several times through a pipette. Vortex thoroughly. The amount of TRIZOL reagent added is based on the area of the culture dish (1 ml per 10 cm2) and not on the number of cells present. An insufficient amount of TRIZOL Reagent may result in DNA contamination of the isolated RNA. Add 0.2 ml of chloroform per 1 ml of TRIZOL Reagent. Cap sample tubes securely. Vortex samples vigorously for 15 seconds and incubate them at room temperature for 2 to 3 minutes. Centrifuge the samples at no more than 12,000 x g for 15 minutes at 2 to 80C. Following centrifugation, the mixture separates into lower red, phenol- chloroform phase, an interphase, and a colorless upper aqueous phase. RNA remains exclusively in the aqueous phase. Transfer upper aqueous phase carefully without disturbing the interphase into fresh tube. Measure the volume of the aqueous phase. Precipitate the RNA from the aqueous phase by mixing with isopropyl alcohol. Use 0.5 ml of isopropyl alcohol per 1 ml of TRIZOL Reagent used for the initial homogenization.

Incubate samples at 15 to 30^{o}C for 10 minutes and centrifuge at not more than 12,000 x g for 10 minutes at 2 to 4^{o}C. The RNA precipitate, often invisible before centrifugation, forms a gel-like pellet on the side and bottom of the tube. Remove the supernatant completely. Wash the RNA pellet once with 75% ethanol, adding at least 1 ml of 75% ethanol per 1 ml of TRIZOL Reagent used for the initial homogenization. Mix the samples by vortexing and centrifuge at no more than 7,500 x g for 5 minutes at 2 to 8^{o}C. Repeat above washing procedure once. Remove all leftover ethanol. Air-dry or vacuum dry RNA pellet for 5-10 minutes. Do not dry the RNA pellet by centrifuge under vacuum. It is important not to let the RNA pellet dry completely as this will greatly decrease its solubility. Partially dissolved RNA samples have an A260/A280 ratio < 1.6. Dissolve RNA in DEPC-treated water by passing solution a few times through a pipette tip.

3.5 Complementary DNA (cDNA) Synthesized

cDNA was synthesized using SuperScript III kit (Invitrogen). The protocol followed the products instruction.

1. Mix and briefly centrifuge each component before use. Preheat the thermal cycler to 65°C.

2. Combine the following in a 0.2–mL, thin-walled PCR tube on ice:

up to 5 µg total RNA: n µL

Primer (50 µM oligo(dT)20, or 50 ng/µL random hexamers): 1 µL

Annealing Buffer: 1 µL

RNase/DNase-free water to 8 µL

3. Incubate in a thermal cycler at 65°C for 5 minutes, then immediately place on ice for at least 1 minute. Collect the contents of the tube by brief centrifugation.

4. Add the following to the tube on ice:

2X First-Strand Reaction Mix: 10 µL

SuperScript III/RNaseOUT Enzyme Mix: 2 µL

5. Vortex the sample briefly to mix, and collect by brief centrifugation. Incubate as follows:

a Oligo(dT)20 or GSP primed: 50 minutes at 50°C

b Random hexamer primed: 5–10 minutes at 25°C, followed by 50 minutes at 50°C

6. Terminate the reactions at 85°C for 5 minutes. Chill on ice.

7. Store the cDNA synthesis reaction at –20°C, or proceed directly to PCR.

3.6 Real time PCR

Real time PCR was performed using Power SYBR Green (Invitrogen) master mix with Applied Biosystems StepOne Plus real time PCR system. The primers used are listed in Table 3. Nox2 gene expression levels were normalized to the housekeeping gene GAPDH.

Table 3: Real-time PCR primers sequence

Gene	Forward primer	Reverse primer
Human Nox2	GCTATGAGGTGGTGATGTTAGT	CTTCAGATTGGTGGCGTTATTG
Mouse Nox2	ACTCCTTGGGTCAGCACTGG	GTTCCTGTCCAGTTGTCTTCG
Mouse TNF-α	CTGTGAAGGGAATGGGTGTT	GGTCACTGTCCCAGCATCTT
Mouse IL-1□	CAACCAACAAGTGATATTCTCCATG	GATCCACACTCTCCAGCTGCA
Mouse IL-6	TTCCATCCAGTTGCCTTCTT	CAGAATTGCCATTGCACAAC

3.7 Intracellular Protein Isolation.

Intracellular protein was isolated according to the following protocol:

1. Place the cell culture dish on ice and wash the cells with ice-cold PBS.

2. Aspirate the PBS, then add ice-cold lysis buffer (1 mL per 10^7 cells/100 mm dish 150 cm^2 flask; 0.5 mL per 5x106 cells/60 mm dish/75 cm^2 flask).

3. Scrape adherent cells off the dish using a cold plastic cell scraper, then gently transfer the cell suspension into a pre-cooled microcentrifuge tube. Alternatively cells can be trypsinized and washed with PBS prior to resuspension in lysis buffer in a microcentrifuge tube.

4. Maintain constant agitation for 30 min at 4°C.

5. Centrifuge in a microcentrifuge at 4°C for 20 min at 12,000 rpm.

6. Gently remove the tubes from the centrifuge and place on ice, aspirate the supernatant and place in a fresh tube kept on ice, and discard the pellet.

3.8 Western Blot

Western blot analysis was performed using previously described protocols established in our group. Briefly, samples containing 40 μg total proteins were separated by electrophoresis on a 1.0% (wt/vol) agarose (molecular biology grade; GIBCO BRL) gels. The electrophoresis buffer [1X Tris-acetate-EDTA (TAE)], contains 0.1% (wt/vol) SDS, 1mM EDTA, and 40mM Tris acetate (pH 8.0). Samples were solubilized in sample buffer consisting of 2.5% (wt/vol) SDS, 4.5 M urea, 5% (vol/vol) β-mercaptoethanol, 25% (vol/vol) glycerol, 0.005% (wt/vol) bromophenol blue, and 0.08 M Tris HCl at pH 7.5. Samples were then denatured at 95°C for 10 minutes and loaded into sample wells in a horizontal gel apparatus (GIBCO BRL). The electrophoresis ran at room temperature at 35 V for several hours, and then at 15 V overnight. Proteins were transferred under positive pressure at 75 mmHg for 2.5 hours from the gel onto a polyvinylidine difluoride (PVDF) membrane (Millipore, Bedford, MA) in a 4X saline- sodium citrate (SSC) buffer made from a 20X stock (Invitrogen). The membrane was allowed to dry overnight (or for at least 2 hours) and then submersed in methanol and rinsed 2X with ddH_2O. The membrane incubated for 1 hour

at room temperature in a milk blocking solution made of 5% non-fat dry milk in 40 mL of 1X PBS containing 0.05% Tween-20 which was added immediately prior to use (PBST). Immunostaining was carried out with the appropriate antibody (see below) in a 2.5% milk blocking solution for 1 hour at room temperature, and then at 4°C overnight. This was followed by secondary immunodetection using an appropriate secondary antibody labeled with horseradish peroxidase for 1 hour at room temperature. Chemiluminescence was carried out using 6 mL (1:1 v/v) of SuperSignal West Dura Chemiluminescent Substrate (Thermoscientific) with a 2 minutes incubation time (manual shaking). The membrane was visualized on Blue Ultra Autrad film (GeneMate). All scans of films are taken using a GS-800 Calibrated Densitometer and ImageJ software.

3.9 Results

To validate each miRNA's ability to suppress human Nox2, we performed luciferase assays in 293T cells cloned with the 3'UTR of Nox2 downstream of luciferase. As shown in Figure 3-1A, all of the three miRNAs significantly decreased luciferase expression

compared to control (miR-106b=78.5±8.6%, P<0.01; miR-148b=78.6±11.1%, P<0.01; miR-204=56.2±8.4%, P<0.001). To determine whether their regulation was conserved, we also validated the selected miRNAs using mouse Nox2 3'UTR downstream of luciferase. Similar to human Nox2, luciferase containing mouse Nox2 3'UTR was also significantly decreased by these miRNAs compared to control group (miR-106b=66,6±6.8%, P<0.001; miR-148b=70.1±8.2%, P<0.001; miR-204=46.7±2.7%, P<0.001, Figure 3-1B).

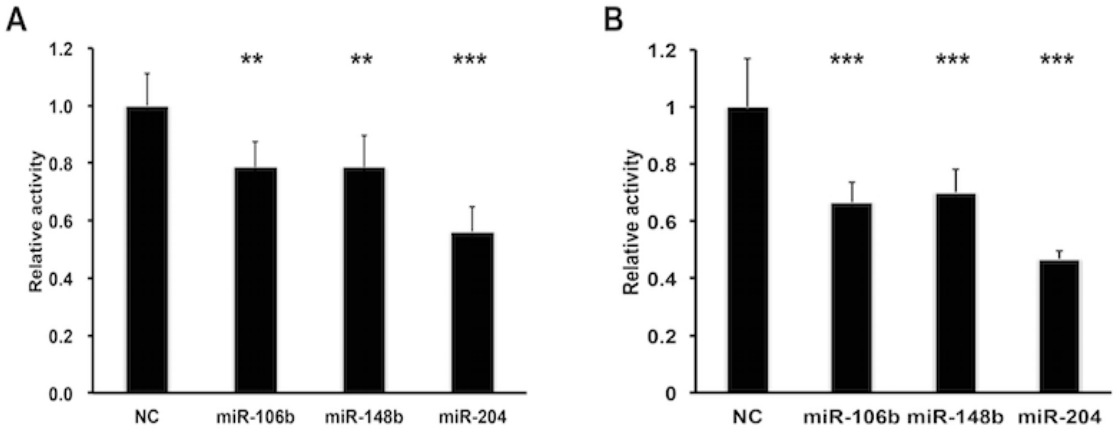

Figure 3-1: miRNAs targeted both humans and mice Nox2. A and B, Relative luciferase activity in Hela cells transfected with indicated miRNAs or control vector with human (A) and mouse (B) Nox2 3'UTR driven reporter constructs, n=5.

We also transfected these miRNAs mimics to induced human macrophages (THP-1 cells) and a mouse macrophage cell line (RAW 264.7). Nox2 mRNA and protein levels were detected by real-time PCR and western blot, respectively. As expected, compared to a

scrambled control miRNA group, all 3 miRNAs decreased both human and mouse Nox2 expression at the gene and protein level by about 40% (Figure 3-2C and D).

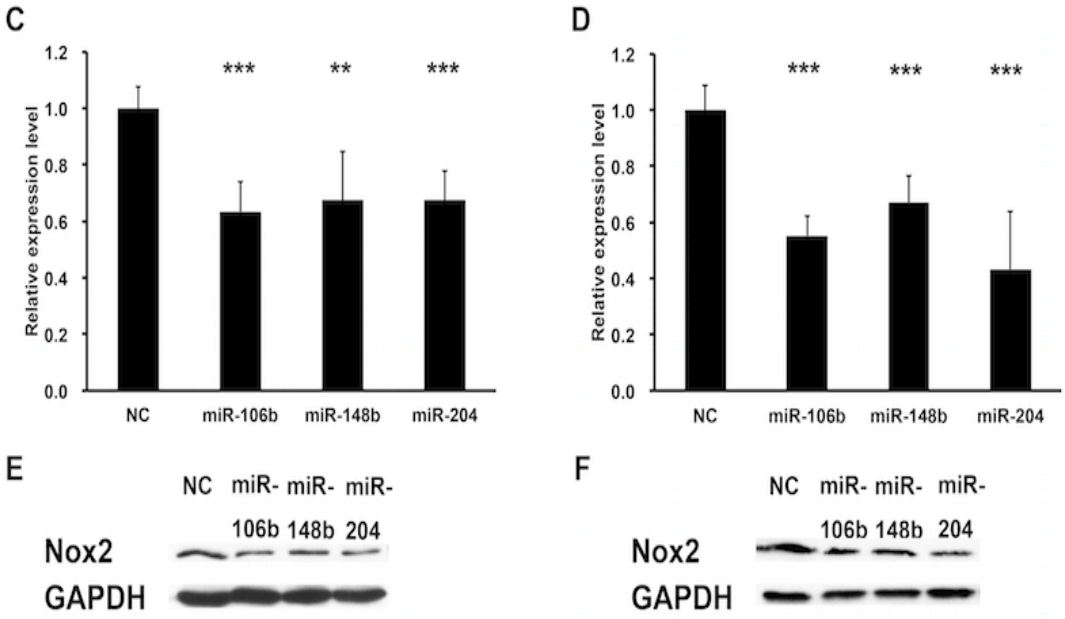

Figure 3-2: miRNAs regulated both humans and mice Nox2 expression. C and D, Real-time PCR for Nox2 in PMA induced THP-1 (C) and RAW 264.7 (D) cells 48 hours after transfection with indicated miRNA or control vector. GAPDH was used as the loading control, n=3. E and F, Immunoblots for Nox2 in PMA induced THP-1 (E) and RAW 264.7 (F) cells 48 hours after transfected with indicated miRNAs or control vector. GAPDH was used as the loading control. **p<0.01; ***p<0.001 (t-test).

CHAPTER 4. IN VITRO FUNCTIONAL KNOCKDOWN OF NOX2 DOWNSTREAM PRODUCTION

4.1 Superoxide Production Staining with Probe

To determine whether Nox2 knockdown by miRNAs resulted in functional changes, we transfected THP-1 induced and RAW 264.7 macrophages with miRNAs separately and 48 hours later, they were stimulated with PMA to induce O_2^- production. ROSstar 650 dye, a fluorescent probe for intracellular ROS, was then added to the cells. Fluorescence intensity was expressed as fold change in O_2^- production normalized to basal O_2^- levels.

4.2 Results

As shown in Figure 4A, after stimulation with PMA, O_2^- production was increased, while each miRNA treatment group showed significantly decreased levels in O_2^- production compared to the control group in THP-1 induced (upper) and RAW 264.7 (bottom) macrophages. Quantification results were shown as Figure 4B for THP-1 induced macrophages and Figure 3C for RAW 264.7 macrophages.

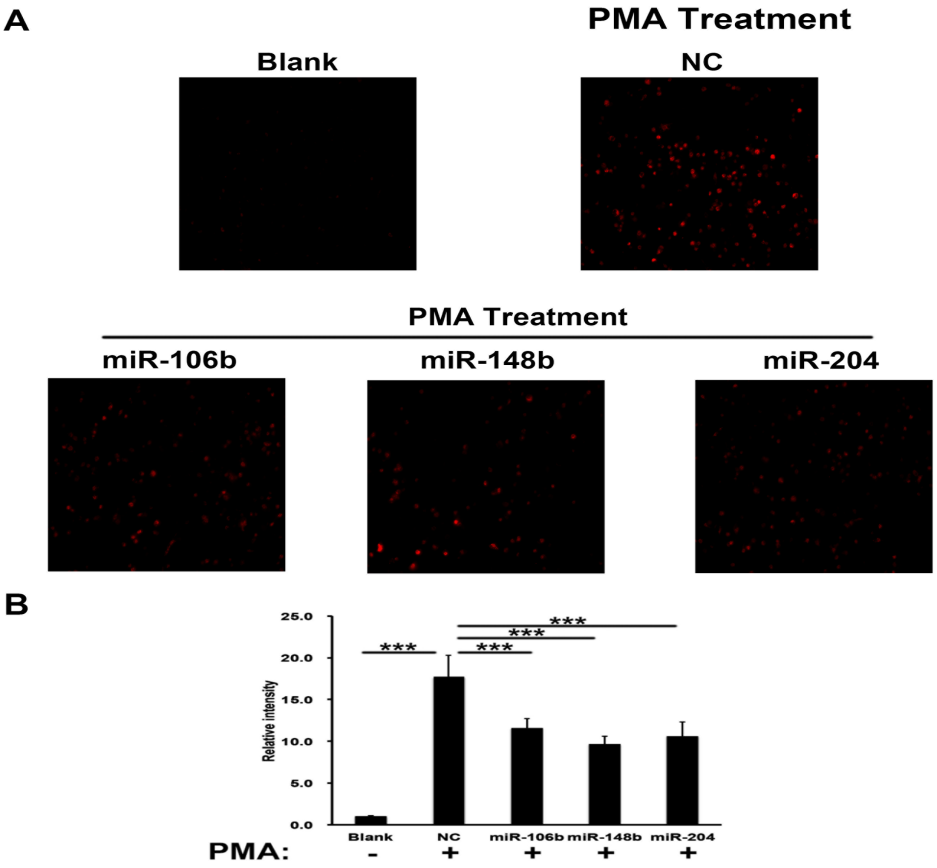
A
PMA Treatment
Blank
NC
PMA Treatment
miR-106b
miR-148b
miR-204
B
Relative intensity
25.0
20.0
15.0
10.0
5.0
0.0
***
***
***
***
Blank
NC
miR-106b
miR-148b
miR-204
PMA:
-
+
+
+
+

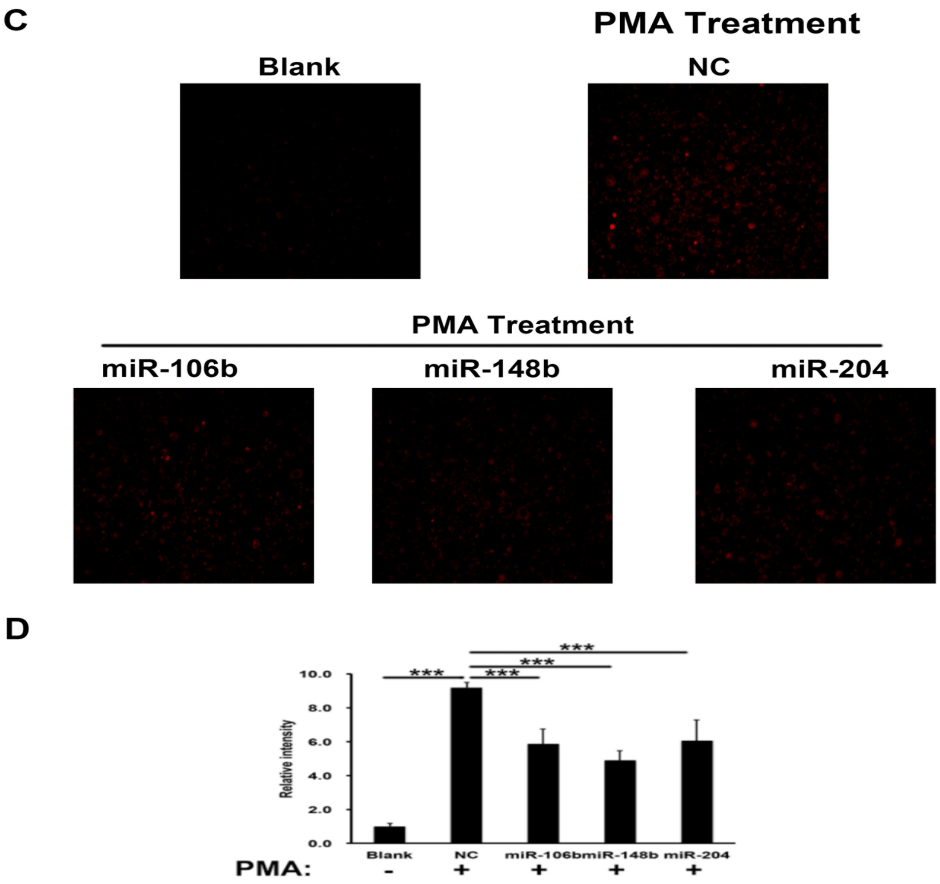

Figure 4: miRNAs inhibited superoxide production in humans and mice macrophages. Superoxide production levels in THP-1 (A) and RAW 264.7 (C) cells were detected with ROSstar dye staining after stimulated by PMA and transfected with indicated miRNAs or control vector, n=3. Scar bar = 100 μm. B and D, Quantification of superoxide production levels in THP-1 (B) and RAW 264.7 (D) cells by comparing fluorescence intensity of indicated group, n=3. ***p<0.001 (t-test).

CHPATER 5. NANOPARTICLE UPTAKE BY MACROPHAGES

5.1 Polyketal (PK3) Synthesis

PK3 was synthesized as described in our prior publications[69]. Briefly, the diols, cyclohexanedimethanol and 1,5-pentanediol were dissolved in distilled benzene and heated to 100°C. Recrystallized p-toluenesulfonic acid (PTSA) was dissolved (~1 mg) in ethyl acetate and added to the benzene solution to catalyze the reaction. The polymerization reaction was initiated by the addition of equimolar 2,2-diethoxypropane (DEP). Additional 2,2-dimethoxy propane (DMP) and benzene were subsequently added to the reaction to compensate for loss of volume in the form of ethanol/methanol and the solvent benzene that had distilled off. After 48 h, the reaction was stopped with triethylamine and isolated by precipitation in cold hexanes. The solid polymer was filtered off, rinsed in hexanes and vacuum dried prior to storage at -20°C. Polymer molecular weight/polydispersity was confirmed by gel permeation chromatography.

5.2 Preparation of miRNA-loaded PK3 particles

PK3-miRNA particles were prepared following the protocol for PK3-siRNA particles[40]. Briefly, 1 mg miRNA in water and 2.2 mg of cationic lipid N-[1-(2,3-Dioleoyloxy)propyl]-N,N,Ntrimethylammonium methysulfate (DOTAP) dissolved in dichloromethane (DCM) were brought to one phase by addition of 1.05 mL of methanol. After 15 min incubation, an additional 0.5 mL of water and DCM were added and the mixture was vortexed, and centrifuged at 750 rpm for 5 min. The miRNA:DOTAP complex in the bottom organic layer was encapsulated in PK3 via an oil/water single emulsion procedure, using DCM as the oil phase and polyvinyl alcohol (PVA) as the surfactant stabilizer. 1 mL of DCM containing ion-paired miRNA was added to 40 mg of PK3 with 1 mg of chloroquine free base. This solution was homogenized into 8 mL of 5% (w/v) PVA solution at the highest setting in the Power Gen 500 (Fisher Scientific) for 30 seconds, and sonicated at an intermediate speed (Sonic dismembrator model 100, Fisher Scientific) with 10 pulses of 1 sec duration. The emulsion was then dispersed in a 20 mL of 0.5% PVA solution and stirred for a period of 4-5 h to allow the DCM to evaporate. The

resulting particles were isolated by centrifugation (15000 rpm, 20 min), washed three times, freeze-dried and stored at -20°C for further use.

5.3 In vitro delivery of PK3-miRNA particles

For in vitro studies, RAW 264.7 macrophages or PMA induced THP-1 cells were plated in 6-well plates at a density of 1 x 10^6 cells per well. After 24 h, cells were treated with indicated PK3-miRNA particles at a concentration of particles equivalent to 2 μg miRNA/well. For gene expression studies, following 48 hours of treatment, the cells were harvested and RNA or protein extracted. For assessment of functional activity of Nox2-NADPH, the cells were kept in wells for analysis of O_2^- production.

5.4 Results

After validation of individual miRNA function on Nox2 expression and downstream O_2^- production, we sought to validate our previously used in vivo delivery system with miRNA in cultured cells. miRNAs encapsulated within PK3 polymer (PK-miRNA) showed similar

loading levels as our prior publications (1 μg per mg particle). Cells were incubated with the indicated PK-miRNA formulation and expression of the delivered miRNA was evaluated with real-time PCR. As shown in in **Figure 5A**, each formulation was able to increase expression of their respective cargo at least 500-fold, indicating effective delivery.

We treated RAW 264.7 macrophages with PK-miRNA particles for 48 hours and Nox2 mRNA expression level was determined by real-time PCR. As shown in **Figure 5B**, treatment with any of the particle formulations significantly reduced Nox2 gene expression (miR-106b=58.9±5.7%, $P<0.001$; miR-148b=63.7±7.9%, $P<0.001$; miR-204=51.1±12.8%, $P<0.001$). O_2^- production was also measured and, similarly to gene expression, treatment with any PK-miRNA particle significantly decreased production as compared to the control group (PK3-NC, **Figure 5C and 5D**).

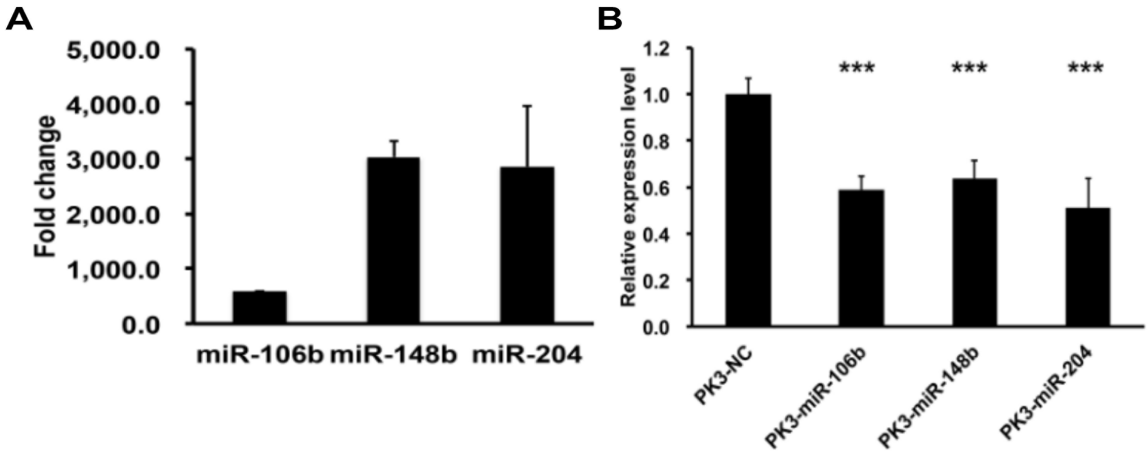

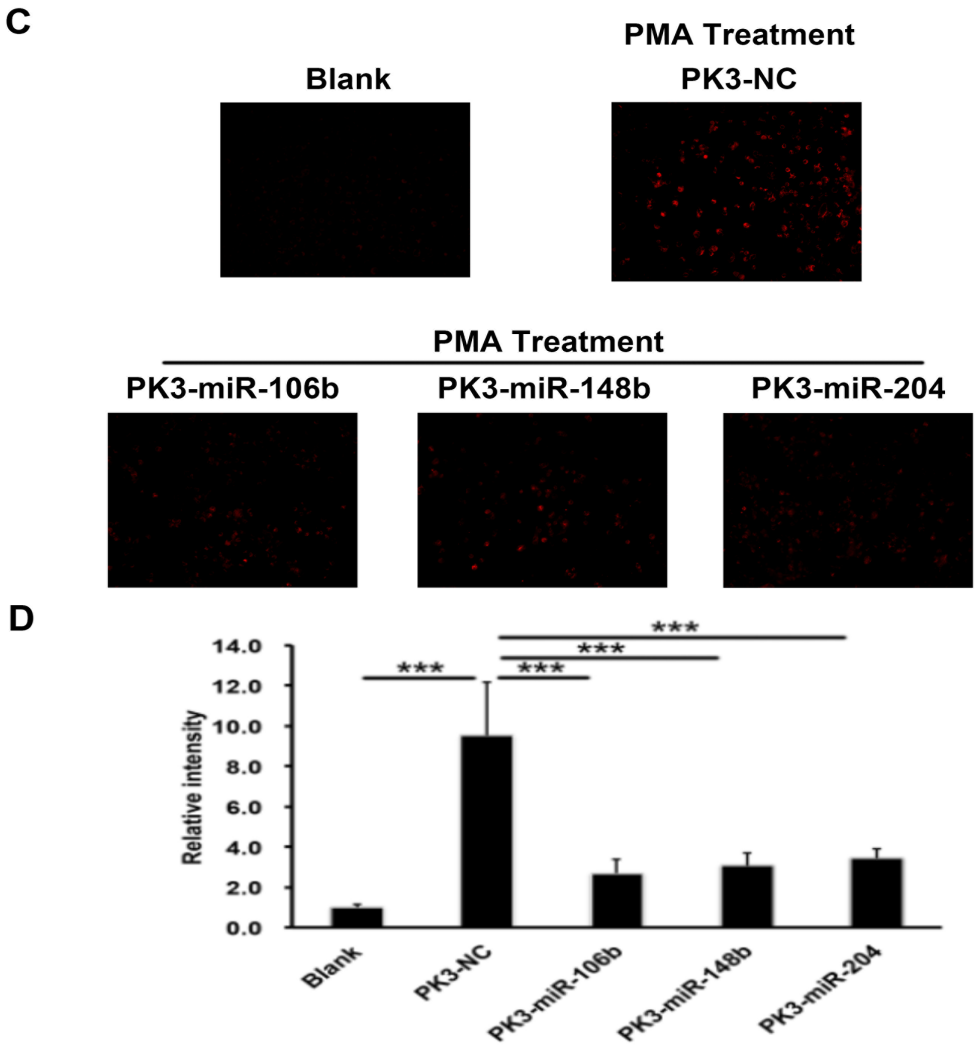

Figure 5: PK3-miRNAs nanoparticles redued Nox2 expression and activity in RAW 264.7 cells. A, Fold change of miRNAs levels in RAW 264.7 cells after treated with indicated PK3-miRNAs nanoparticles by real-time PCR. U6 was used as the loading control, n=3. B, Real-time PCR of Nox2 in RAW 264.7 cells after treatment with indicated PK3-miRNA or control nanoparticles. GAPDH was used as the loading control, n=3. C and D, Representative images (C) and quantification (D) of superoxide production levels in RAW 264.7 cells treated with indicated nanoparticles by ROSstar dye, n=3. ***p<0.001 (t-test).

CHPATER 6. PK3-MIRNAS NANOPARTICLES IN VIVO DELIVERY

6.1 Myocardial Infarction and Particle Injection

Studies were conducted under a randomized and blinded manner. Adult male C57BL/6 mice (>8 weeks) were used and assigned to five groups. One group was subjected to sham surgery, while the other four groups received permanent myocardial infarction. The surgeries were conducted as described previously[68]. Briefly, the animals were anesthetized by isoflurane. Following tracheal intubation, the heart was exposed by separation of the ribs. Myocardial infarction was achieved by ligation of the left anterior descending coronary artery. For mice getting particle injections, 50 μL of indicated particle was injected into the cyanotic ischemic zone through a 30-gauge needle immediately after ligation. The dose of miRNA injected was 5 μg/kg. After injection, the chests were closed and animals were recovered on a heating pad. Functional assessments were made at 3 days following surgeries using echocardiography. These studies conformed to the Guide for the Care and Use of Laboratory Animals published by the US National Institutes of Health and all animals studies were approved by Emory University Institutional Animal Care and Use Committee.

6.2 Immunohistochemistry

Fresh heart tissue was frozen in Tissue-Tek OCT and 5 μm sections were made. After washing with PBS, sections were fixed by 4% formaldehyde solution an then incubated with goat serum for 1 h. Nox2 antibody diluted in goat serum was added to the sections and incubated at 4°C overnight. After that, sections were washed 3 times using PBS-Tween and incubated with fluorescent secondary antibody for 2 h at room temperature. Nuclei were stained by Hoechst dye. Images were taken by Nikon at identical exposures and analyzed by ImageJ software.

6.3 Echocardiography

Anesthetized mice were subjected to echocardiography 3 days after MI surgery. Short axis values of left ventricular diameter were obtained using a Vevo 770 small animal ultrasound system (Visualsonics). An average of 3 consecutive cardiac cycles was used for each measurement and performed three times in an investigator-blinded manner. Fractional

shortening (FS) was calculated as (end-diastolic diameter – end-systolic diameter)/end-diastolic diameter and expressed as a percentage.

6.4 Results.

To determine the in vivo efficiency of miRNA mediated-Nox2 suppression, adult male C57BL/6 mice were randomized into 5 treatment groups. Control mice were subjected to sham surgery, while the other four groups received MI surgery followed by injection of PK-miRNA or a negative control scrambled miRNA particle (PK-NC). At 3-days post injury, hearts were harvested and expression of Nox2 was determined by immunofluorescence staining of frozen sections. As shown in **Figure 6-1A and B**, there was a significant increase in Nox2 staining with PK-NC treatment following MI as compared to sham mice (about 3-fold, $P<0.001$). Compared to PK-NC group, each PK-miRNA treatment group demonstrated significantly reduced staining of Nox2 (miR-106b=43.2$\pm$6.8%, $P<0.001$; miR-148b=24.8$\pm$6.3%, $P<0.001$; miR-204=35.9$\pm$5.1%, $P<0.001$). Additionally, O_2^- levels were determined by DHE staining on

frozen sections. Similar to Nox2 expression levels, each PK-miRNA treatment significantly reduced the elevated DHE staining at least 50% (**Figure 6-1C and D**).

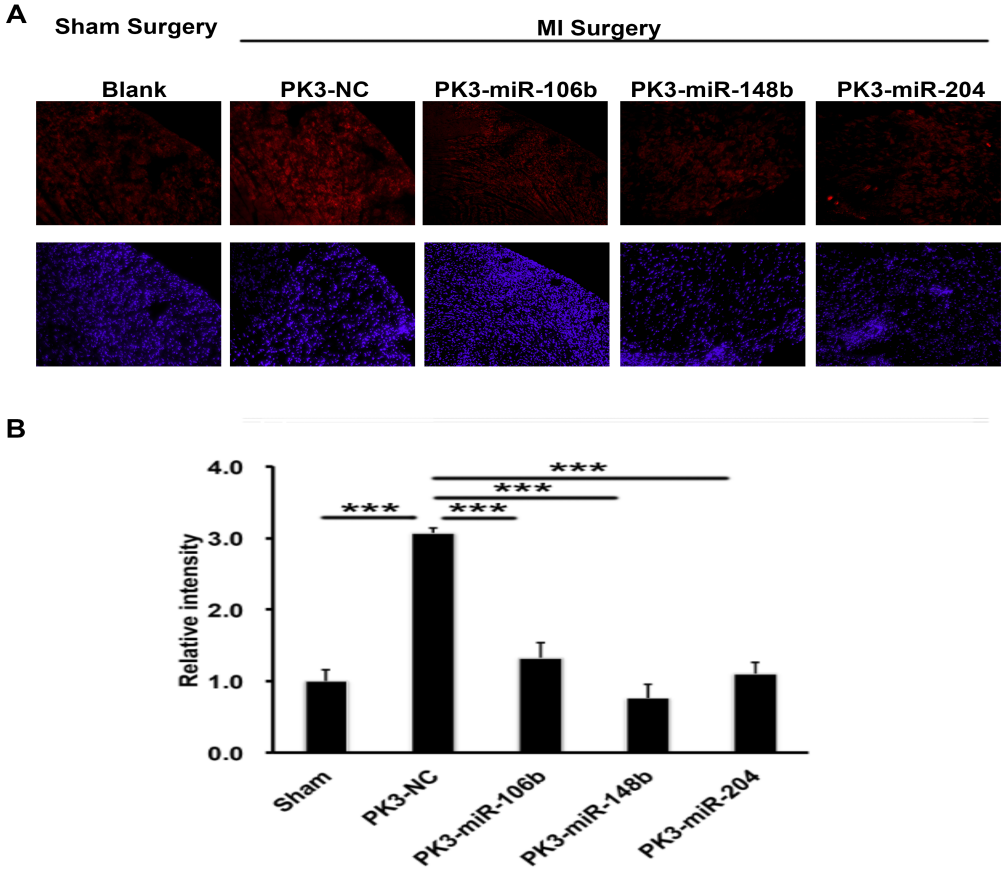

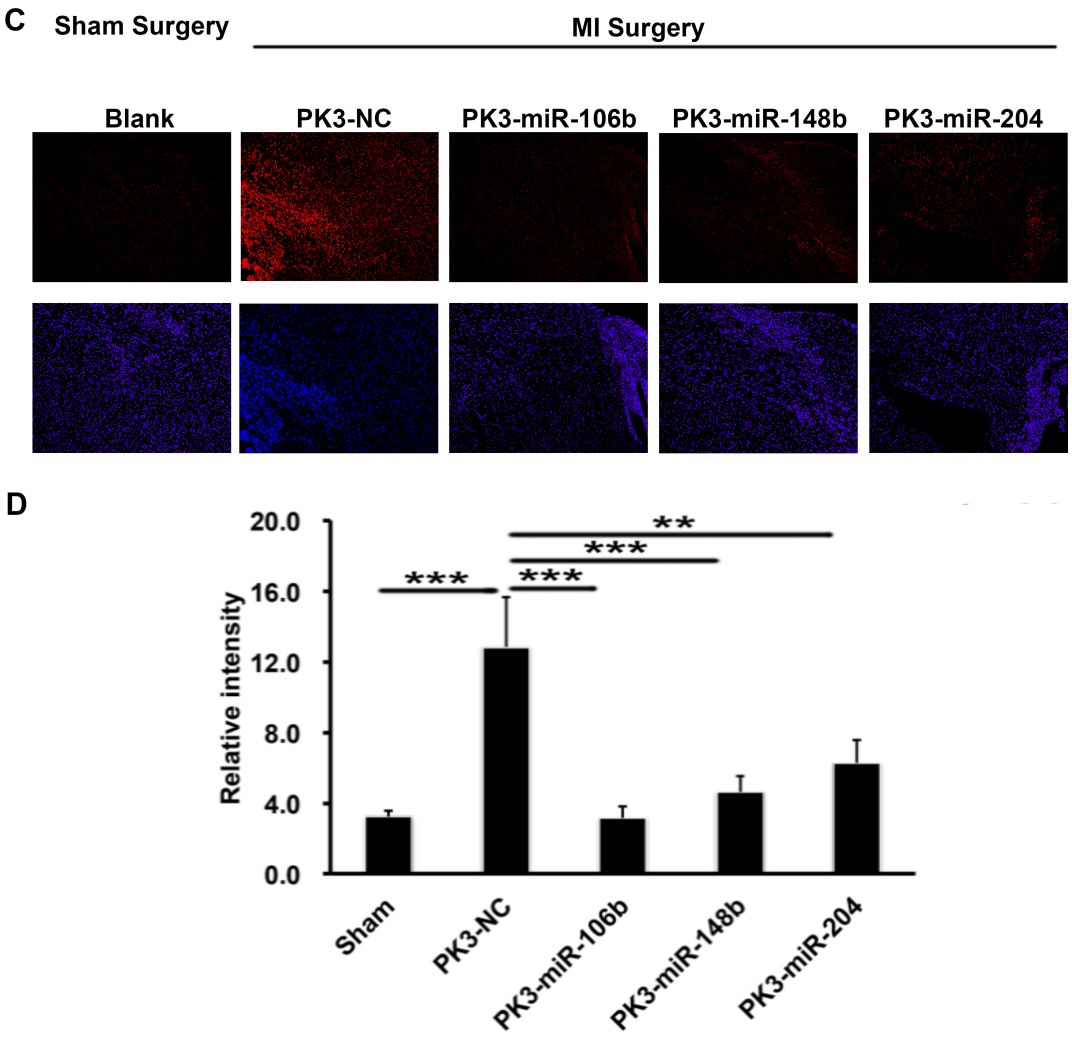

Figure 6-1: PK3-miRNAs nanoparticles inhibited Nox2 expression and activity in vivo. A and B, Representative images (A) and quantification (B) of Nox2 (red) levels by in situ immunostaining on frozen sections from indicated treatment mice heart tissues. Cell nuclei were stained by Hoechst (blue), n=5. C and D, Representative images (C) and quantification (D) of superoxide production levels by DHE staining on frozen sections from indicated mouse heart tissues. Cell nuclei were stained by Hoechst, n=5. Scar bar = 100 μm. **p<0.01; ***p<0.001 (t-test).

To determine the effect of PK-miRNAs delivery on acute cardiac function after MI, echocardiography data was collected 3 days after injury. As shown in **Figure 6-2A, B and C**,

MI significantly reduced cardiac function as measured in absolute change in fractional shortening and ejection fraction 3 days post-injury. Treatment with each PK-miRNA particle significantly improved function, restoring it to sham levels.

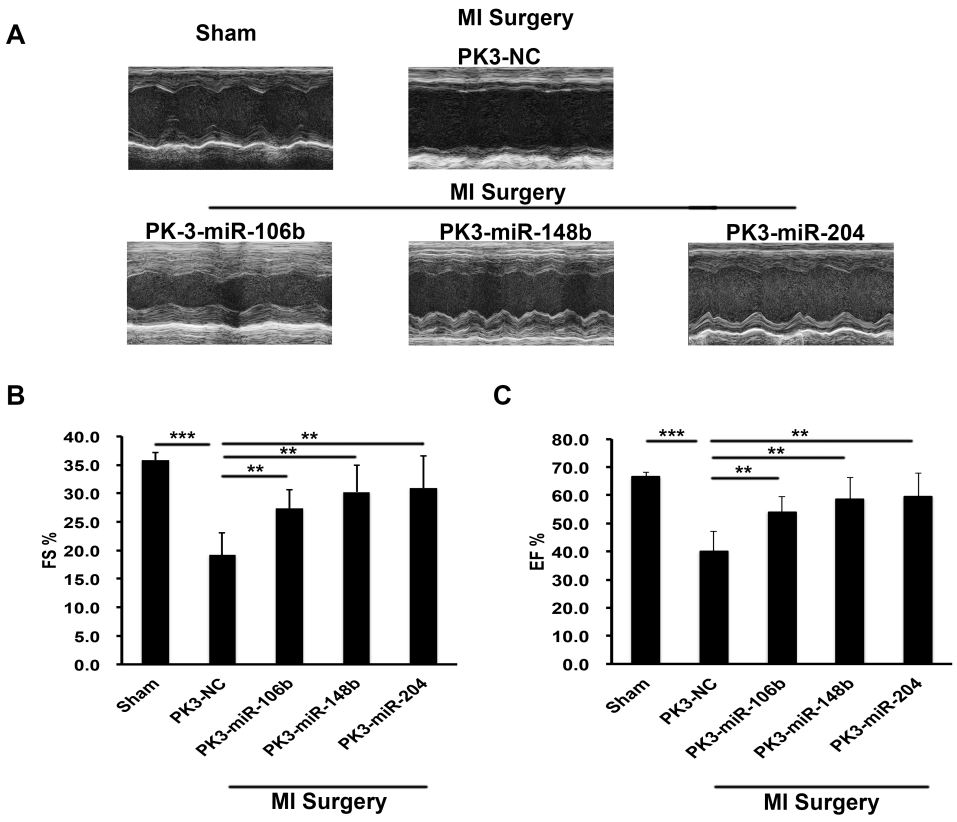

Figure 6-2: PK3-miRNA nanoparticles improved cardiac function after MI. A, Echocardiographic pictures of mice 3 days after indicated treatment. B and C, Echocardiographic parameters Fractional shortening (B) and Ejection fraction (C) from indicated group of mice, n=5. **p<0.01; ***p<0.001 (t-test).

CHPATER 7. DISCUSSION

Substantial evidence shows that oxidative stress due to excessive ROS such as O_2^- plays an important role in the development of post-MI cardiac dysfunction[70-71]. Antioxidant treatment following MI in animal models improves cardiomyocyte survival, attenuates ventricular remodeling, and results in preservation of left ventricular function[72]. NAPDH oxidases are major sources of O_2^- in the heart and the family of gp91 proteins (Nox 1-5) is an important catalytic unit of the NADPH oxidase[71]. Nox2 is mainly expressed in macrophages, fibroblasts, endothelial cells and cardiomyocytes[73] and is significantly increased in the myocardium following MI with the massive influx of inflammatory cells[74-75]. Nox2 is also increased in human cardiomyocytes following MI[75]. Nox2 knockout mice are protected from post-MI dysfunction[39], and studies from our own laboratory show that siRNA against Nox2 encapsulated in nanoparticles can protect against acute MI dysfunction[40]. Therefore finding additional was to target Nox2 could be a promising therapeutic approach for preserving function following acute MI.

In the current report, we successfully identified several miRNAs targeting Nox2 with the use of a high-throughout miRNA-target screening system and validated their targeting using a luciferase reporter system with the 3'UTR of Nox2. We also confirmed their function by testing Nox2 expression and function in both human and mouse macrophage cell lines. To date, there had been no studies that identified a miRNA that directly bound the Nox2 3'UTR and decreased expression. The SAMcell assay provided a straightforward way to identify miRNAs that target a specific gene. In our previous studies, the performance of this system had been demonstrated using a phenotypic approach to determine miRNAs that regulated processes involved in cancer[63]. In this study, miRNAs were selected that were conserved between human and mouse in order to test potential human targets in mouse models of MI. Three specific miRNAs were chosen for more detailed analysis due to prior publications underscoring their involvement in post-MI healing. Following MI, miR-106b reduced apoptosis via inhibition of p21 expression[76], and has also been shown to target the pro-inflammatory cytokine IL-8[77]. The second hit, miR-148b, has been reported to negatively regulate LPS-induced cytokine production in dendritic

cells, including IL-6, IL-12, and TNF-a, and plays an important role in immune regulation[78]. In addition, a significantly decreased expression of miR-148b was observed in isoproterenol-induced myocardial injury and fibrosis; expression was increased when apocynin treatment was used to reverse this[79]. Finally, our third hit, miR-204, was decreased after ischemia-reperfusion (IR) injury in mice and overexpression of miR-204 protected the cardiomyocytes against IR-induced autophagy[80].

After selection of these three miRNAs, their inhibition of both human and mouse Nox2 was validated by several methods. Luciferase assays using the Nox2 3'UTR demonstrated they could each decrease Nox2 expression directly by canonical miRNA regulation. Real-time PCR and western blot studies confirmed that all three miRNAs decreased Nox2 levels at the gene and protein levels (Figure 3-2). DHE staining for PMA-induced superoxide levels (a surrogate of Nox2 activity) also showed the functional benefit of the miRNA-induced decrease in Nox2 levels. There was no significant additive effect by delivery of all

three miRNAs together compared to the single miRNA alone both for Nox2 expression level and O_2^- production level as shown in Figure 7-1 and 7-2.

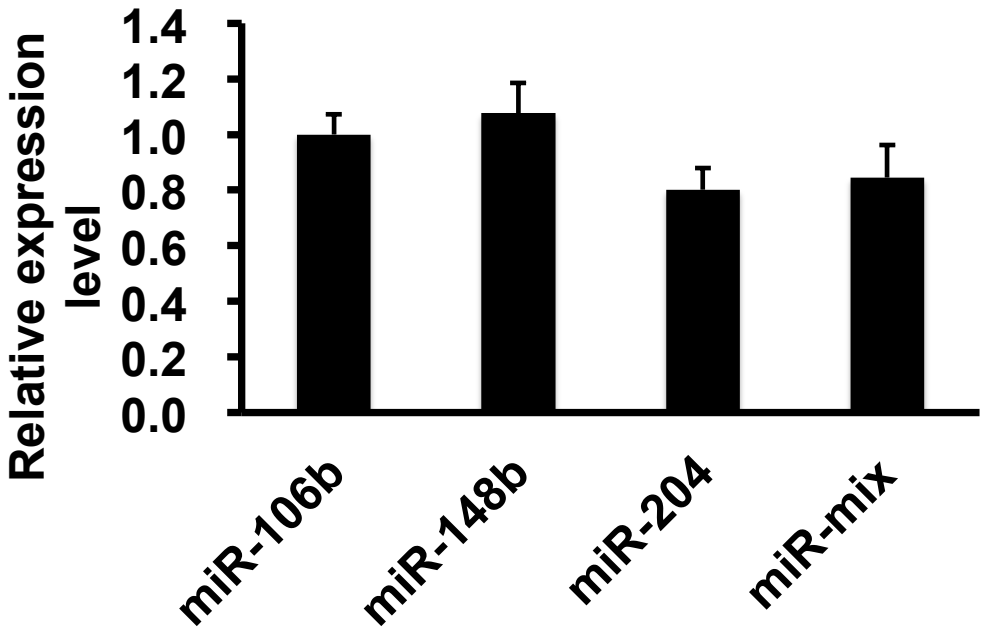

Figure 7-1: Comparison of inhibition effects on Nox2 by miRNAs. Real-time PCR for Nox2 mRNA in RAW 264.7 after transfection with indicated miRNA or a mixture of all 3 miRNAs normalized to miR-106b treatment. Data show no difference between individual miRNAs or combinations, n=3 ($p>0.05$, t-test).

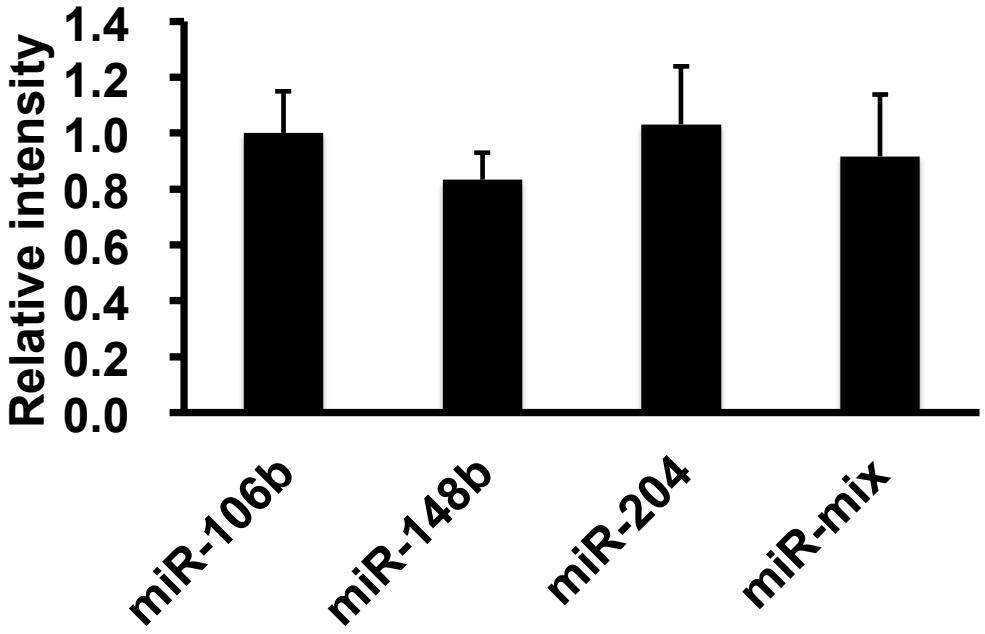

Figure 7-2: Combination of three miRNAs did not have additive effect on Nox2 activity. Quantification of relative fluorescence intensity with DHE staining in RAW 264.7 after transfection with indicated miRNA, result of miR-106b used as control. No significant difference among four groups, n=3. ($p>0.05$, t-test).

Once miRNAs were selected and validated, we sought to utilize an efficient delivery system for targeting macrophages in vivo. Polyketals are a class of delivery vehicles formulated from a class of polymers that contain pH-sensitive, hydrolyzable ketal linkages in their backbone. We had used the polyketal PK3 to deliver miRNA to bone marrow mononuclear cells to induce pluripotency[32]. There was no difference in miRNA transfection efficiency between commercial transfection reagent (Oligofactamine) and PK3 nanoparticles

(Figure 7-3). Additional published studies from our laboratory demonstrated that PK3 nanoparticles were retained in the myocardium after injection and could be used to deliver siRNA following MI in mice[40]. When engaged by macrophages, particles were taken up into phagosome/endosomes where they degrade due to the acidic environment, leading to release of cargo into the cytoplasm of macrophages (over 80% transfection efficiency). In that study we successfully delivered Nox2 siRNA into cardiac macrophages by PK3 particles and observed a significant improvement in heart function after MI.

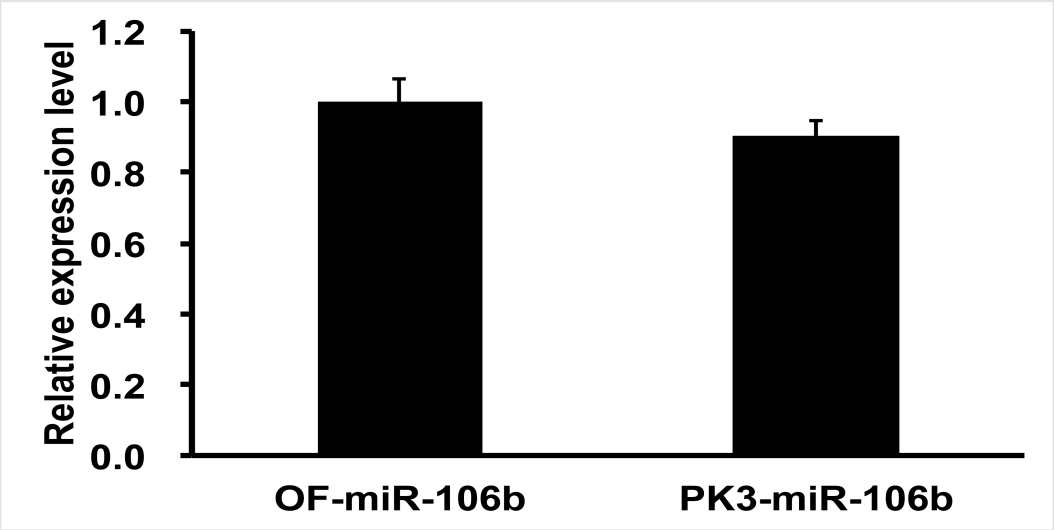

Figure 7-3: Comparison of miRNA transfection efficiency between Oligofectamine and PK3 nanoparticles. Real-time PCR for miR-106b in RAW 264.7 after transfection equal

amount of miR-106b by Oligofectamine (OF-miR-106b) and PK3 nanoparticles (PK3-miR-106b), n=3. p>0.05 (t-test).

Despite our prior study showing beneficial effects of delivery of siRNA to Nox2, delivery of miRNA might have potential advantages. Firstly, miRNA is more natural as there is no siRNA in mammalian cells. miRNA is viewed as endogenous and purposefully expressed products in an organism's own genome, whereas siRNA is thought to be primarily exogenous in origin, derived directly from viruses, transposons, or transgene triggers[81]. Additionally, introduction of too much siRNA could result in nonspecific events due to activation of innate immune response[82]. Secondly, miRNA could target many genes and sometimes from the same pathways. For example, let-7, which was shown to be able to directly regulate some key cell cycle proto-oncogenes, e.g., RAS, CDC25a, CDK6, and cyclin D at the same time, was a key regulator of cell proliferation[83]. Likewise, miR-23b plays an important role in tumor metastasis since it regulates a cohort of prometastatic targets, including FZD7, MAP3K1, TGFBR2 and PAK2[84]. To validate this hypothesis in this study, we examined expression levels of other pro-inflammatory genes such as IL-1 β ,

IL-6 and TNF-a by real-time PCR in RAW 264.7 macrophages after transfection with miRNAs. As Figure 7-4, 7-5 and 7-6 shown, these miRNAs significantly decreased the mRNA expression level of these pro-inflammatory genes as well, except miR-204 on TNF-a.

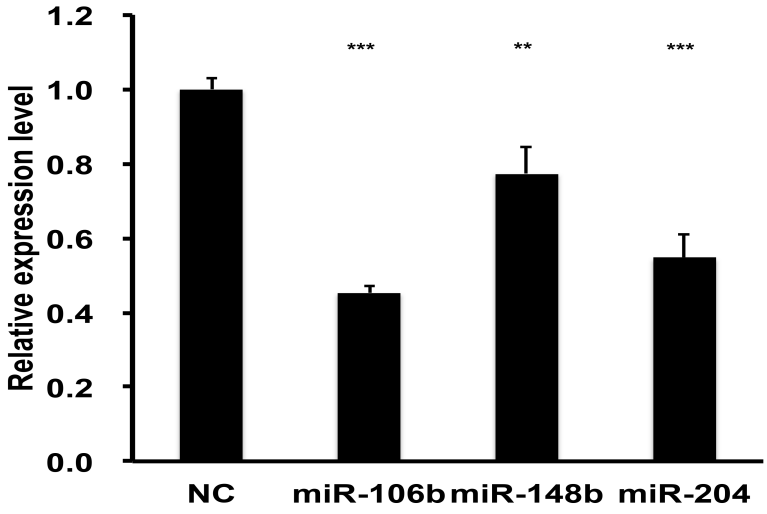

Figure 7-4: Identified miRNAs inhibited IL-1β expression. Real-time PCR for IL-1β mRNA in RAW 264.7 after transfection with indicated miRNA. n=3. **p<0.01, ***p<0.001 (t-test).

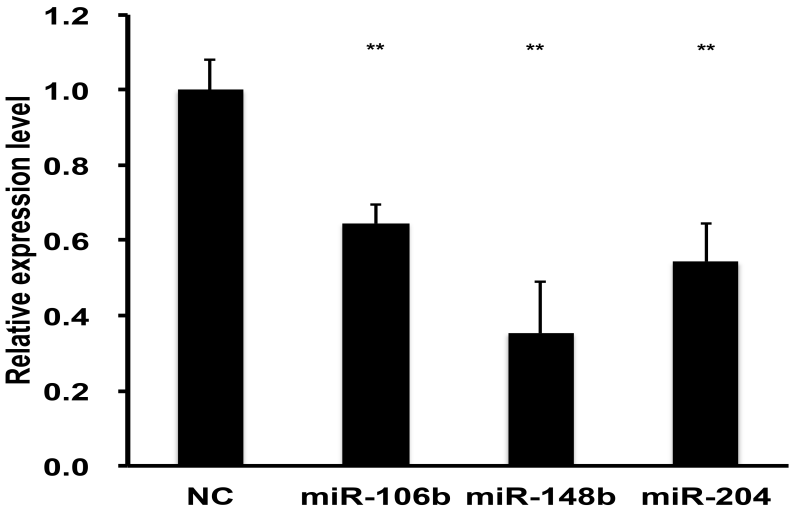

Figure 7-5: miRNAs inhibited IL-6 expression. Real-time PCR for IL-6 mRNA in RAW 264.7 after transfection with indicated miRNA. n=3. **p<0.01 (t-test).

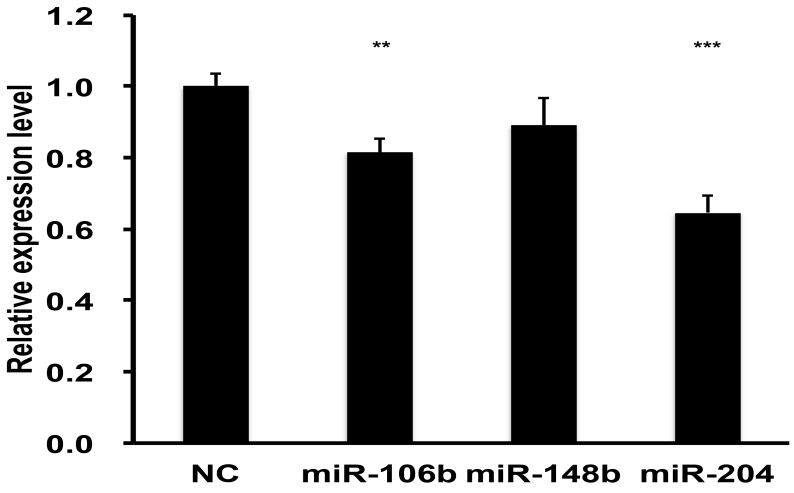

Figure 7-6: miRNAs inhibited TNF-α expression. Real-time PCR for TNF-α mRNA in RAW 264.7 after transfection with indicated miRNA. n=3. **p<0.01, ***p<0.001 (t-test).

We next examined the efficacy of these particles in vivo, in a mouse model of MI. Similar to our prior studies, we delivered particles immediately following ligation to the border zone of the infarct. In keeping with published studies[37-39], both Nox2 levels and superoxide levels were significantly increased following MI (Figure 4B and 4D). While Nox2 levels have been shown to be upregulated in cardiomyocytes, most staining indicated non-cardiomyocyte origin, likely infiltrating inflammatory cells. While we did not identify the source of the superoxide, it was also likely inflammatory cells based on prior studies[71-72]. While it is possible that Nox2 was increased in myocytes, our published studies show that polyketals are not efficiently taken up by cardiomyocytes without surface modification of the nanoparticles[69, 85]. It would be interesting to encapsulate the miRNAs in these modified particles and determine whether miRNA-mediated knockdown of Nox2 in cardiomyocytes is sufficient for protection, though this would be unlikely due to the large influx of inflammatory cells. Additionally, we did not measure other ROS such as hydrogen peroxide (H_2O_2), which could also mediate damage. The role of H_2O_2 in acute MI is controversial and it remains a debate as to whether this is a valid target as H_2O_2 is also

involved in important physiological processes. It is also likely that reduced levels of O_2^- also resulted in decreases in H_2O_2 and understanding this balance could be an interesting topic for future consideration. After treatment with any PK3-miRNA, Nox2 expression and O_2^- levels were reduced significantly compared to the empty particle group. More importantly, an improvement in cardiac function was observed in each PK3-miRNA formulation treatment group. These results corroborated reports that knockdown of Nox2 improves cardiac function after MI.

In conclusion, we have found novel miRNA regulation of Nox2 expression by utilizing a high throughput miRNA-target screening method, the SAMcell assay, to narrow down potential targets, specifically miR-106b, 148b, and 204. We validated the results in transfected cells, as well as human and mouse macrophages. Combined with our efficient macrophage-specific delivery approach, these miRNAs were able to reduce Nox2 expression and activity in vivo, resulting in improved acute function. With the robust nature of these

systems, other inflammatory molecules can be studied to determine optimal miRNA candidates to modulate inflammation in vivo.

CHPATER 8. FUTURE WORK

Despite the promising results from this study, there are still lots of work need to be completed in the future. First of all, only three miRNAs are selected from the screening results. We need to demonstrate if other miRNAs can inhibit Nox2 as well, or even with better effects. Furthermore, in order to move this PK3 nanoparticles delivery system into clinical applications, we need to test this system in more animal models, such as porcine and non-human primate model. Finally, as macrophages play a significant role in lots of inflammation related diseases, we can expect this delivery system to be functionally utilized in other disease models.

CHPATER 9. OTHER PROJECT DURING PH.D. PROGRAM: BIOCOMPATIBILITY ASSESSMENT OF DETONATION NANODIAMOND IN NON-HUMAN PRIMATES USING URINE, HEMATOLOGIC, AND HISTOLOGICAL ANALYSIS

9.1 Summary

Detonation nanodiamonds (DNDs) have been widely studied for various applications in biomedical area, including magnetic resonance imaging and cancer therapy. They have several unique properties, such as faceted surfaces that mediate water coordination and drug binding. These give DNDs significantly enhancements in the efficiency and safety in imaging and drug delivery. In addition, DNDs have been shown to be well-tolerated by many biocompatibility studies. Consequently, there is a high demand for comprehensive assessment of DND safety in large animal preclinical models. Here we demonstrated a DND biocompatibility study in non-human primates. This non-human primate study was performed as a multiple dose, dual gender and long-term observation in both standard/clinically relevant and elevated dosing cohorts that lasted for six months and included comprehensive urine, serum, histological, and body weight analysis. The results from these studies indicate that DNDs are well-tolerated at

clinically relevant doses and examination of dose-dependent changes in biomarker levels provides important directions for the following in-human validation of DNDs for clinical imagin and drug delivery.

9.2 Introduction

9.2.1 Nanodiamonds

Nanodiamond particles produced by detonation were first discovered in the 1960s[86], while they kept unknown to most of the world until the end of the 1980s[87]. After that, a series of significant breakthroughs were achieved that leading to a broader interests in these particles. First of all, it became available to get individual diamond particles in colloidal suspensions with diameters of 4-5 nm[88]. Meanwhile, fluorescent nanodiamonds were used by investigators as a non-toxic alternative for imaging in biomedical field[89]. Finally, researchers demonstrated that nanodiamonds were less toxic compared to other carbon nanoparticles[90-91], which largely broader their applications areas.

Nowadays, there are various kinds of nanodiamonds available for research. The technologies used to synthesized nanodiamonds include detonation technique, lase ablation[92], plasma-assisted chemical vapour deposition[93], ion irradiation of graphite[94] and ultrasound cavitation[95].

9.2.2 Synthesis of Nanodiamonds

Nanodiamonds can be manufactured by explosives in moleculars. This method provides a source of carbon and energy for the conversion as well. The detonation happens in a closed chamber filled with an inert gat or water coolant, called dry or wet synthesis, respectively. The product, detonation soot, is a mixture of diamond particles with 4-5 nm in diameter and other carbon allotropes and impurities. These impurities can be inside the nanodiamond aggregates or outside their surfaces. For industrial applications, liquid oxidants are used to purify detonation soot.

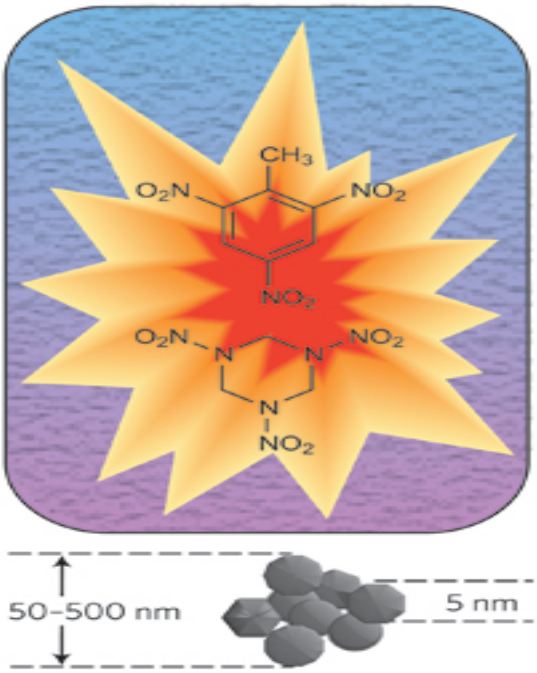

Figure 9-1: In order to synthesize nanodiamonds, explosives with a negative oxygen balance (for example a mix of 60 wt% TNT ($C_6H_2(NO_2)_3CH_3$) and 40 wt% hexogen ($C_3H_6N_6O_6$)) are detonated in a closed metallic chamber in an atmosphere of N_2, CO_2 and liquid or solid H_2O. After detonation, diamond-containing soot is collected from the bottom and the walls of the chamber.

9.2.3 Properties of Nanodiamonds

Nanodiamond is a kind of excellent material in many respects, including superior hardness and Young's modulus, biocompatibility, optical properties and fluorescence, electrical resistivity, chemical stability, and great thermal conductivity.

Fluorescent particles can be produced by linking[96] or adsorbing[97] different fluorophores into the nanodiamonds. These conjugated nanodiamonds can go through cellular compartments without affecting cell viability and degradation of fluorophore for quite a long time. Fluorescent nanodiamonds combine the advantages of semiconductor quantum dots, such as small size, high photostability, multicolor fluorescence, with biocompatibility and non-toxicity. This property gives them the potential application for in vivo imaging applications[98]. Quite a lot of studies have been made to demonstrate nanodiamonds affects on cell viability, gene expression activity, and in vivo mechanistic and physiological behavior[99-100]. Nanodiamonds were reported to be of low pulmonary toxicity and intravenously administered nanodiamonds complexes did not change serum indicators of liver, even at high dosages[101].

9.2.4 Applications of Nanodiamonds

A good drug delivery system requires properties include biocompatibility, dispersability and the capability to carry different therapeutics. Also the potential for targets therapy is important. Nanodiamonds are able to meet most of these requirements[102-103]. Studies have

demonstrated the efficacy and safety of nanodiamonds-mediated delivery in mice[104]. Nanodiamond-doxorubicin complexes (ND-Dox) were validated to treat drug-resistant breast cancer and liver cancer models. The complexes reduced the capacity of the tumors. Meanwhile, the half-time of circulation ND-Dox was 10 times that of unmodified doxorubicin. Besides of delivering small molecules, nanodiamonds were investigated to deliver nucleic acids when coated with polyethylenimine 800 (PEI 800)[102]. There was a 70-fold increase of GFP plasmid transfection efficacy and an increased efficacy over commercial transfection reagent when used for siRNA delivery[103].

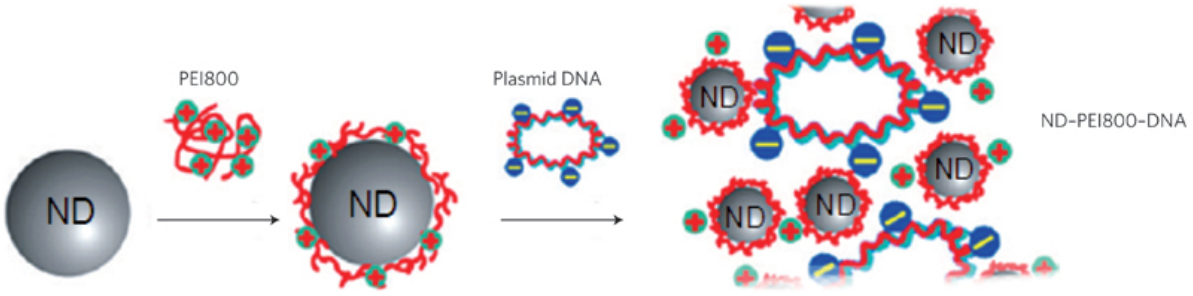

Figure 9-2: DNA can be electrostatically attached to nanodiamonds by first covering negatively charged carboxylated nanodiamonds with positively charged PEI800

molecules. A similar electrostatic binding strategy has been used to attach siRNA and doxorubicin (Dox) to nanodiamond.

There are increasing interests in the areas of tissue engineering and regenerative medicine. It has been shown that nanodiamond monolayers can be used as a platform for neuronal growth[104]. The great mechanical properties, including tunable surface chemistry, drug delivery ability, and biocompatibility, make nanodiamond be able to create functional tissue engineering scaffolds. One reported application is ND-ODA-PLLA composite. It did not affect morphology and proliferation when used for culturing murine 7F2 osteoblast. These composites have clinically relevant properties and being non-toxic.

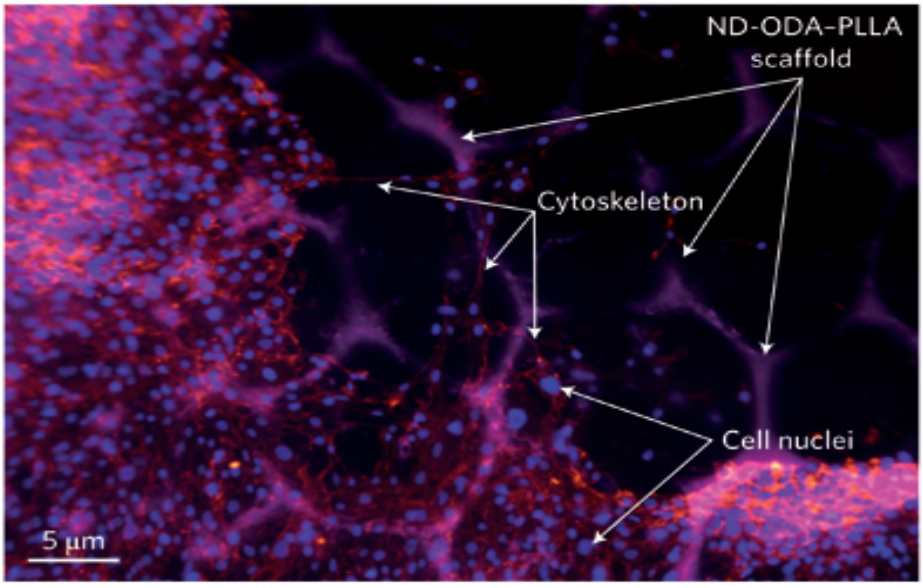

Figure 9-3: ND–ODA can be used for bio-imaging, as illustrated by this confocal micrograph of the fluorescent scaffold made of ND–ODA–PLLA with 7F2 osteoblasts grown on it.

9.3 Methods for Detonation Nanodiamond Administration in A Non-human Primate Model

9.3.1 Non-human Primate Care and Identification

Cynomolgus monkeys of both genders were used for the study. Their ages ranged from three to six years. Three control subjects were used for the study. All the animals were maintained by Kunming Biomed International. The control ones were assigned by the following numbers: 071691(M), 071837(M), and 071669(M). The test subjects given a standard dose of DNDs (15 mg/kg) were assigned identifier numbers 080118(F), 071079(M), 070473(M), 070476(F), and 080410(F). Test subjects receiving an elevated dose of DNDs (25 mg/kg) were assigned identifier numbers 071425(M), 071805(M), 070696(F), and 070508(F).

Animals were provided with controlled rooms compliant with animal welfare guidelines. The environment was maintained as temperature (18-26^{o}C), humidity (30-70%), air circulation, and light-dark cycle (12/12 hours). Monkeys were fed with a welfare guideline-compliant commercial monkey diet. Adverse events were defined as conditions that the monkeys displayed any indication of obvious toxicity or intolerance of DNDs.

9.3.2 Non-human Primate Dosing Protocol

Each monkey received 6 doses of DNDs at either 15 or 25 mg/kg. Blood and urine samples were obtained before each administration and used as the baseline. Three weeks after the last administration, blood and urine samples were collected again. The whole treatment lasted for duration of six months.

9.3.3 Non-Human Primate Serum and Urine Analysis

Serum and urine samples were obtained using conventional equipment and procedures that have been previously outlined[105]. Serum chemistry, complete blood count, urinalysis,

weight monitoring, and observation period assessment were conducted to comprehensively characterize test subject health.

9.3.4 Non-Human Primate Histopathology Analysis

Immediately after euthanasia, tissues were harvested and fixed in 10% neutral-buffered formalin for at least 48 hours. Then samples were dehydrated in increasing concentrations of ethanol and embedded in paraffin wax. Tissues were made into sections that were 4–5 μm thick and adhered to positively charged glass slides. Sections were stained with hematoxylin and eosin for evaluation. All slides were evaluated using a Nikon Eclipse 80i upright microscope (LHS-N100C-1, Nikon Instruments Inc., Japan).

9.3.5 Statistics

All analyses were performed in GraphPad Prism using two-way ANOVA using the Bonferroni correction for multiple comparisons. A repeated measures analysis was used for the

non-human primate studies to take into account between subject variations. Data were considered significant at $p < 0.05$.

9.4 Results

9.4.1 Body Weight Analysis after DNDs Administration

During the period of the study, all the groups were monitored for body weight and appetite. No obvious acute or sustained fluctuations in animal body weight were discovered during the study period. There were no apparent changes to animal appetite either. These results indicated that DNDs administration did not cause severe systemic toxicity or adversely affect the digestive systems. This is critically important for clinical applications.

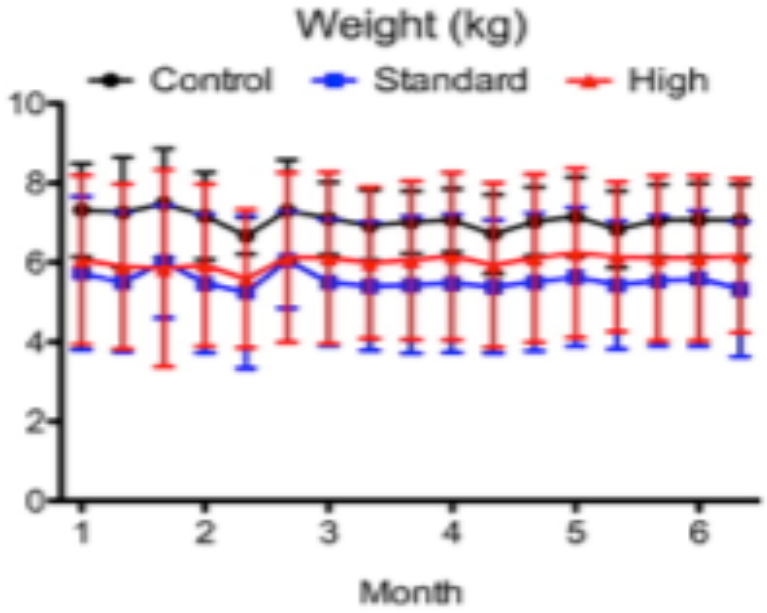

Figure 9-4: Weights of monkeys treated with indicated amount of detonation nanodiamonds or controls. No significant difference was identified.

9.4.2 Complete Blood Count Analysis after DNDs Administration

A complete blood account was regarded as a standard clinical practice. It was used to assess the overall health and screen for inflammation, toxicity, and hemolysis and any other side effects. Overall, he platelet count (PLT) was the only hematological parameter that had statistically significant variation. One week after doses 2, 5, and 6, samples had higher PLT in the control group, compared to the other two groups. It should be notice that PLT readings had

great fluctuations in all animals. It was more likely that the difference was due to an increase in the reads of control group, rather than a decrease in the treatment groups. The values from treatment groups were consistent with their baseline before treatment.

Red blood cell distribution width (RDW-CV, 14.75 ± 1.28%) was assessed and red blood cell counts (RBC, 6.22 ± 0.45 × 10^{12}/L) were also evaluated as part of the complete blood counts. No substantial deviations were investigated in all the test subjects, except the one 070473, whose RDW-CV reading was elevated compared to its starting and ending levels. It was shown negligible fluctuations for Hematocrit (HCT, 48.98 ± 2.94%) levels. Mean corpuscular volume (MCV, 78.84 ± 3.34 fL) had higher values at the end of treatment. Mean corpuscular hemoglobin (MHC, 22.81 ± 1.11 pg) readings showed very little fluctuation within each test subject. And mean corpuscular hemoglobin concentration (MCHC, 289.49 ± 10.46 g/L) analysis exhibited a generally decreasing trend for all the subjects that converged toward the normal range.

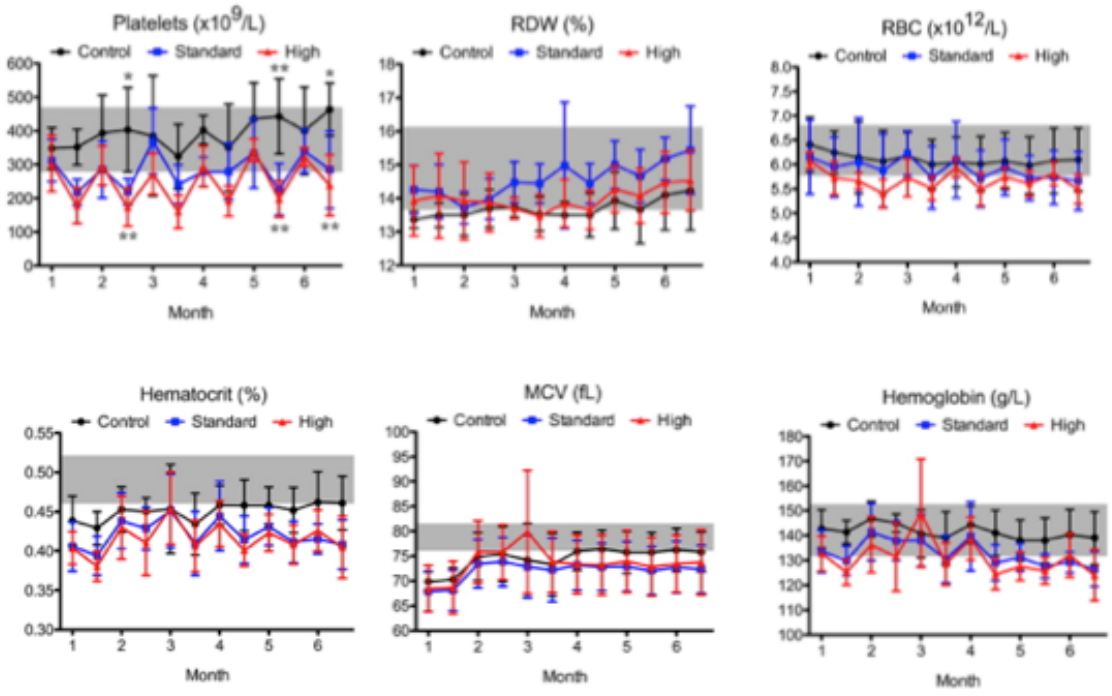

Figure 9-5: Hematologic parameter analysis of monkeys treated with detonation nanodiamonds. Monkeys were treated monthly with either a standard dose (15 mg/kg) or a high dose (25 mg/kg) of DNDs. Blood was sampled prior to each treatment and 1 week after treatment. Statistically significant differences in platelet count were noted at multiple time points (*p < 0.05, **p < 0.01). All other parameters were non-significant.

Taken together, it was demonstrated by these discoveries that the nanoparticle infusions did not make the test subjects experience a hemolytic response or be anemic.

We also measured white blood cell counts (WBC, 13.31 ± 4.41 × 10^9/L) and neutrophil counts (NEU, 6.43 ± 3.72 × 10^9/L, 46.66 ± 14.37%). Although measurements in all the test subjects exhibited substantial fluctuations, we did not find any apparent increasing or depression trends

in any of these levels. Large standard deviations were observed with the reference level standards for lymphocyte counts (LYM, 6.00 ± 2.38 × 10^9/L, 45.96 ± 13.20%). We did not observe any trends in the values of WBC, NEU, and LYM, while some of them were under the expected normal range.

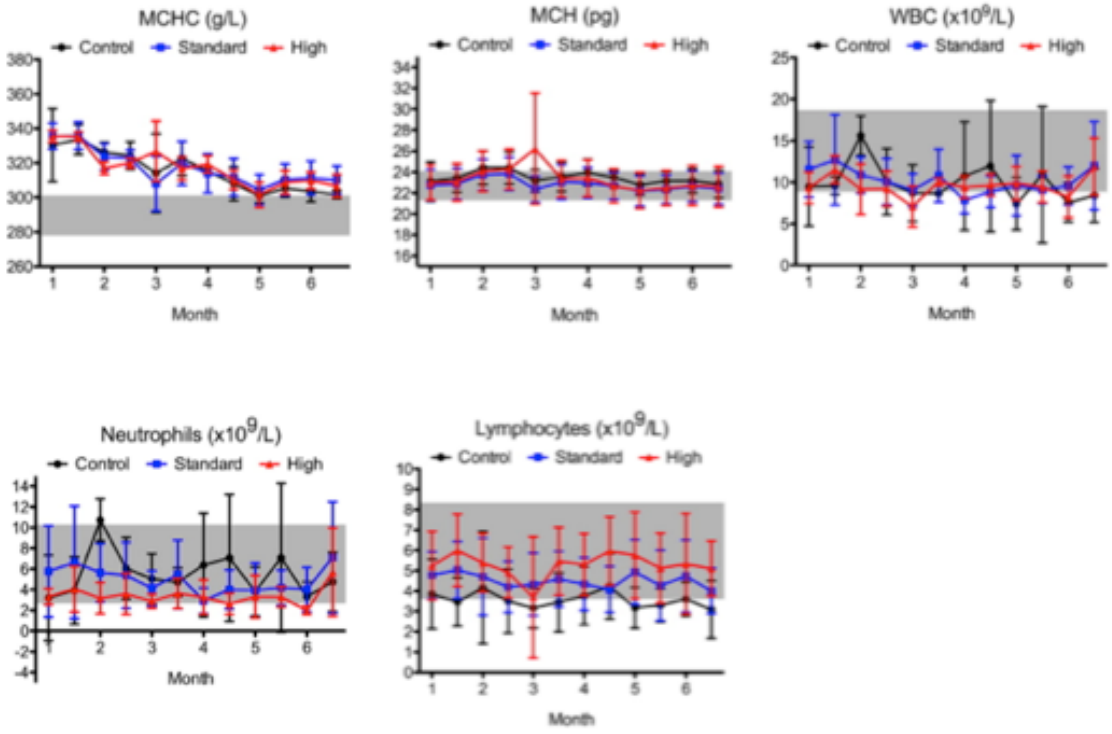

Figure 9-6: Hematologic parameter analysis of monkeys treated with detonation nanodiamonds. Monkeys were treated monthly with either a standard dose (15 mg/kg) or a high dose (25 mg/kg) of DNDs. Blood was sampled prior to each treatment and 1 week after treatment. All other parameters were non-significant.

These data provided significant insight about the overall health of the test subjects. No trends were observed that were attributable to DND administration, although occasional fluctuations were found in marker levels during the study. In addition, all subjects maintained their weight during the entire study. The DND administration was demonstrated to be well tolerated as there was no clear anemia, inflammatory response, or toxicity.

9.4.3 Urinalysis Following DND Administration

We assessed urine from all subjects at the same time points with the hematologic analyses. Previous reference studies provided the reference values for urinalysis in cynomolgus monkeys. For one time point, urine pH readings showed that subjects 071079(M/S), 070473(M/S), 080118(F/S), and 071425(M/E) each reached a urine pH level of 9. However, all of these subjects finished the treatment with normal urine pH values. None of these subjects had urinary tract infections, as urine nitrite tests came back negative. Almost all test subjects had negative urine glucose (uGLU) readings. One control subject (071691(M)) and one treatment subject (070508(F/E)) tested positive for uGLU at one time point each.

However, both subjects completed the study with negative uGLU. All subjects had normal levels of urobilinogen and were negatively tested for urinary bilirubin, except subject 071805(M/E). There were two times of positive reading for that subject, but completed with negative tests. All subjects were found to have transiently positive urine protein levels (uPRO), indicating that protein presence was unlikely due to DND treatment.

There was at least once during the entire study that tested positive for urine leukocytes and erythrocytes (uLEU, uERY) for all subjects. It is usually considered normal for healthy subjects when uLEU levels are low. There was no statistically significant difference between standard treatment group and control group in the average uLEU levels. Similarly, there were no any significant trends for uERY values.

Finally, substantial variability in all urine electrolytes (sodium, potassium, chloride, and calcium) was observed. There were no significant trends in any of these for all groups. Furthermore, no evidence of kidney infection or damage was observed during the study. Taken together, both the liver and kidneys of all subjects were functioning normally proved by the

urinalysis data. In addition, there were no significantly differences in the results between the standard and elevated group.

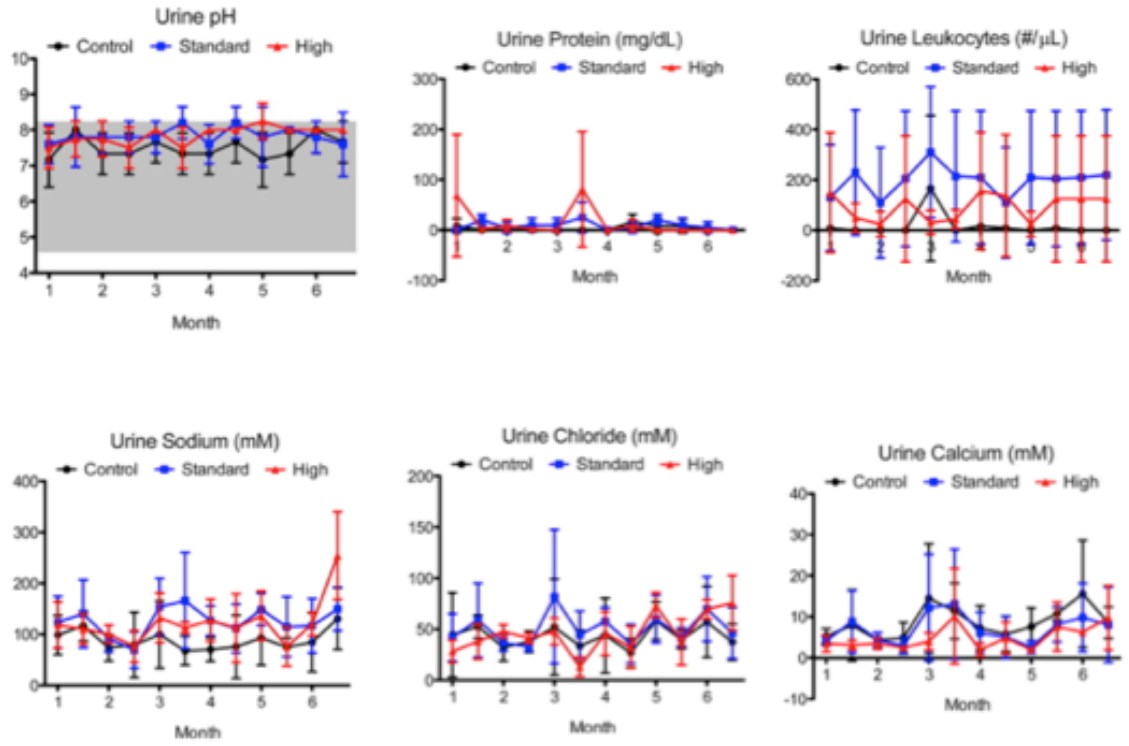

Figure 9-7: Urinalysis of monkeys treated with detonation nanodiamonds. Monkeys were treated monthly with either a standard dose (15 mg/kg) or a high dose (25 mg/kg) of DNDs. Blood was sampled prior to each treatment and 1 week after treatment. No statistically significant variations in parameters were observed.

9.4.4 Non-human Primate Histopathology Analysis

One control (071691(M)), two standard dose monkeys (080118(F) and 071079(M)), and two elevated dose monkeys (070696(F) and 071425(M)) were used to conduct tissue analysis. Tissue from the lung, heart, liver, kidney, and spleen were stained with hematoxylin and eosin. We did not identify any gross abnormality in both the standard and elevated groups compared to the controls. Heart sections from elevated group showed increased muscle fiber hypertrophy compared to the controls, while there was only mild changes in sections from standard group. Evidence of prominent capillary congestion and dilatation compared to the control animals was found in the liver parenchyma from the elevated group, while standard ND dose monkeys had similar but less advance changes in morphology. Compared to control group, there were no significant morphologic changes in kidneys and spleens in standard and elevated group.

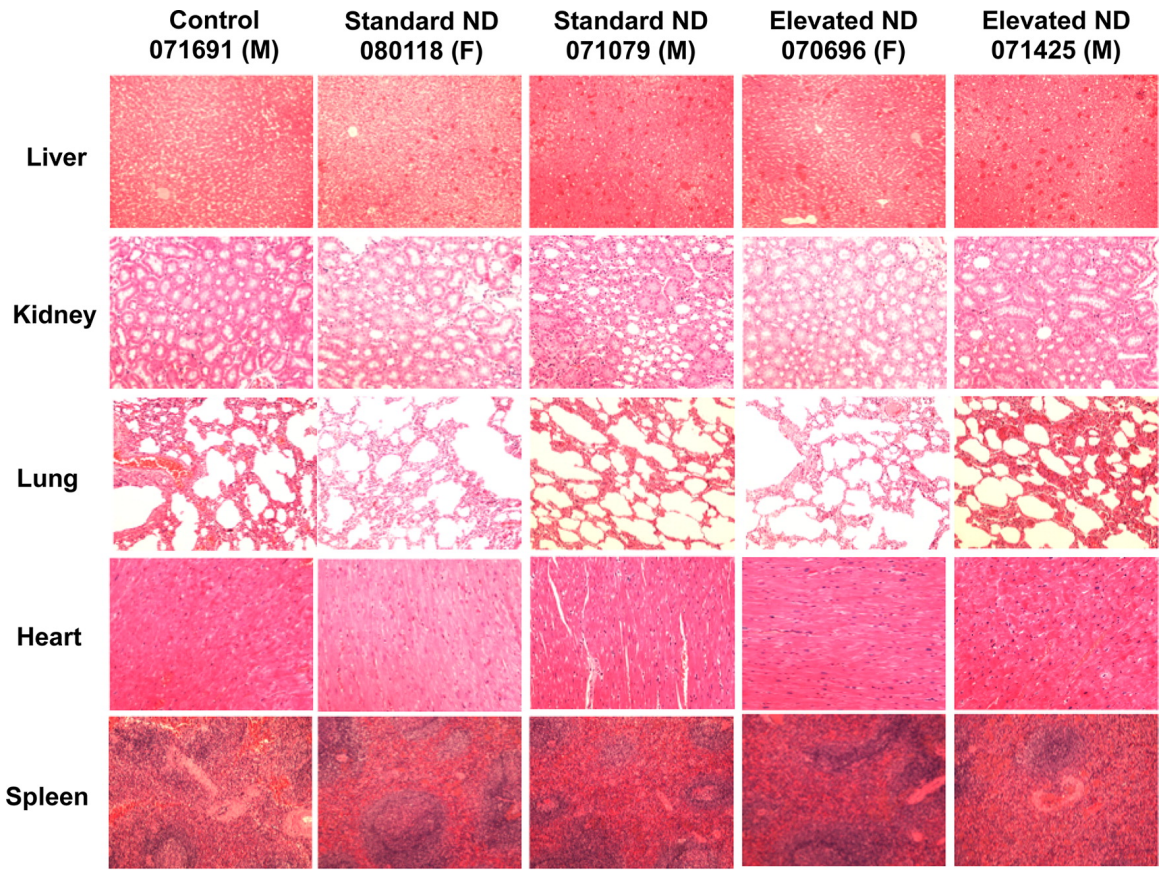

Figure 9-8: Histologic analysis of monkeys treated with detonation nanodiamonds. Monkeys were treated monthly with either a standard dose (15 mg/kg) or a high dose (25 mg/kg) of DNDs. Tissue samples from the liver, kidney, lung, heart, and spleen were obtained at 6 months from control, standard dose (both genders), and elevated dose (both genders) for analysis.

9.5 Conclusion

This study demonstrated significant insight into the biocompatibility of DND preclinical administration in a non-human primate model. The results provided in this study are

comprehensive, including DND safety characterization, long study period, and repeated dosing scheme. Both genders of cynomolgus monkeys had been evaluated with two DND dosing levels, a standard dose of 15 mg/kg (n=5) and an elevated dose of 25 mg/kg (n=4), in addition to controls (n=3). This study gave important insight into no apparent adverse effect level and maximum tolerated dose of DND administration. The estimated clinical DND monotherapy dosage will be between 6.75 and 13.5 mg/kg. Furthermore, combination therapy technologies will optimize DND-containing multidrug treatment and further reduce the DND and drug dosage. Consequently, both 15 and 25 mg/kg in our study serves as a foundation for clinical translation of DND-based therapeutic and contrast agents. Completion of non-human primate histology is required to further confirm material tolerance. In addition, to establish in-human validation protocols, comprehensive pharmacokinetic analysis and the development of chemistry, manufacturing, and controls compliance are demanded.

9.6 Discussion

The area of nanomedicine has made strides to the improved diagnosis and treatment of various diseases, such as cancer and infectious diseases[106-107]. However, progress has been

limited as the result of the costs related to drug development. Therefore, in the context of the area of drug development, it's important to select specific carriers, indications, and drugs. Among those promising carriers that have been applied in nanomedicine, detonation nanodiamonts (DNDs) have recently received increasing attention due to their abilities in photostable cell labeling, drug delivery, and medically imaging[109-110], as a result of their faceted surfaces and uniform particle structure. In particular, DNDs are able to potently binding anthracyclines and sustaining their release with no need for modification either the DND surface or the drug itself[111]. These DND-anthracycline complexes are capable of improving drug tolerance and maximally efficacious tumor reduction using drug dosages that are lethal when delivered on their own. In the area of medically related imaging, DNDs are used to carry gadolinium(III) (Gd(III)), leading to a one order of magnitude increase in per-G(III) relaxivity for magnetic resonance imaging (MRI) applications[112]. This is among the largest increase ever reported for per-gadolinium relaxivity, compared to all nanoparticle and clinical MRI contrast agents.

To test nanodiamond (ND) biocompatibility, investigators have used different cell lines and animal models platforms for several informative studies[111, 113, 114]. These studies were largely demonstrated with in vitro, ex vivo, or small animal models. Consequently, to continue developing of ND for clinical administration requires the assessment of their tolerance in large animal models with comprehensive blood and urine analysis. Furthermore, the implementation of a dual gender and long-term large animal study is vital because of the fact that differences can exist between male and female subjects. To achieve this goal, we performed our study on non-human primate animals, in which male and female cynomolgus monkeys were administered an intravenous injection once a month for a period of six months. Two cohorts were each administered either a standard (15 mg/kg) or elevated (25 mg/kg) DND dose, while blood and urine draws were systematically acquired for comprehensive toxicity analysis. At the conclusion of the dosing protocol, the animals were subsequently entered into an observation phase to assess visible changes to their health and monitor possible weight changes. The results demonstrated that the DNDs were well-tolerated for the duration of non-human primate animals and also provided important insights as to the maximum tolerated dose

(MTD) and the “no observed adverse effect level”. Therefore, these studies provide and important foundation for the nonclinical risk assessment of DND-based therapies and imaging agents as they progress into potential in-human validation.

APPENDIX

Full screening results for human Nox2

miRNA-	Fold Change	P-value
106b	0.9000	0.0003
148b	0.9010	0.0001
21	0.9049	0.0191
miR-135b	0.9150	0.0004
296-5p	0.9155	0.0005
590-5p	0.9209	0.1019
33a	0.9233	0.0289
let-7f-1-3p	0.9250	0.0498
29c*	0.9258	0.0037
let-7i	0.9265	0.0268
204	0.9278	0.0082
221	0.9315	0.1212
190	0.9337	0.1169
miR-7	0.9355	0.0581
331-3p	0.9362	0.0463
301a	0.9406	0.0099
let7a	0.9422	0.1556
200c*	0.9433	0.1158

494	0.9447	0.0159
491-5p	0.9472	0.0073
708	0.9477	0.0015
let-7c	0.9478	0.0461
542-3p	0.9498	0.0007
133a	0.9513	0.1503
331-5p	0.9535	0.0103
188-5p	0.9536	0.0056
let-7f	0.9537	0.0355
29a*	0.9540	0.0792
124*	0.9540	0.1559
24	0.9558	0.0815
216b	0.9562	0.0568
744-3p	0.9580	0.4949
16	0.9659	0.1308
100	0.9615	0.3914
874	0.9617	0.2782
499-5p	0.9617	0.0254
15b	0.9625	0.2871
125b	0.9625	0.2915
93*	0.9641	0.0194

1	0.9653	0.2942
miR-144	0.9657	0.1095
183	0.9657	0.1553
574-3p	0.9662	0.1014
196b	0.9683	0.1769
132	0.9685	0.4838
137	0.9686	0.0185
208a	0.9691	0.0077
27a-5p	0.9691	0.0458
296-3p	0.9694	0.1267
431	0.9695	0.4896
323-3p	0.9702	0.0507
9	0.9704	0.4396
361-5p	0.9709	0.4448
miR-200b	0.9711	0.1925
184	0.9713	0.1015
miR-139-5p	0.9720	0.0842
381	0.9726	0.1005
223	0.9727	0.3162
133b	0.9731	0.2680
188-3p	0.9732	0.0624
let-7g	0.9733	0.1763

127-3p	0.9741	0.2307
98	0.9742	0.0148
miR-760	0.9747	0.3794
342-3P	0.9752	0.3902
33a*	0.9760	0.4122
146a	0.9768	0.0637
425	0.9769	0.0798
761	0.9770	0.4737
708*	0.9770	0.0333
153	0.9775	0.2021
187	0.9775	0.6121
551b	0.9779	0.0597
10a*	0.9780	0.3615
568	0.9785	0.0693
504	0.9786	0.3578
638	0.9789	0.3961
494	0.9789	0.4309
744	0.9790	0.1181
543	0.9792	0.4803
223	0.9793	0.0184
455-5p	0.9794	0.0258

448	0.9795	0.5576
183*	0.9796	0.4285
490-3p	0.9796	0.0792
377	0.9798	0.4623
129*	0.9800	0.1372
181a	0.9803	0.1631
30a*	0.9813	0.4639
30a	0.9814	0.1431
103	0.9817	0.4634
485-5p	0.9819	0.2796
484	0.9821	0.3347
129-5p	0.9825	0.0232
323-5p	0.9831	0.2398
652	0.9836	0.0852
29a	0.9840	0.0149
1197	0.9841	0.6098
340-3p	0.9845	0.3283
93	0.9847	0.1879
330-5p	0.9849	0.7557
10b	0.9851	0.4565
369-5P	0.9857	0.5503
miR-152	0.9863	0.5410

miR-149	0.9876	0.4327
141	0.9880	0.6568
324-5P	0.9882	0.5936
574-5p	0.9884	0.4634
338-3p	0.9886	0.5254
154*	0.9888	0.6294
140-5p	0.9892	0.6354
181d	0.9896	0.4508
129-3p	0.9898	0.5787
423-5P	0.9901	0.7107
29c	0.9902	0.2705
34c-5p	0.9907	0.6926
22-5p	0.9907	0.6013
miR-200c	0.9910	0.4198
30c-1*	0.9911	0.7678
miR-25	0.9917	0.7257
671-3p	0.9918	0.2629
210	0.9921	0.8800
23a	0.9922	0.4062
20b	0.9923	0.4854
32	0.9924	0.3872

138	0.9924	0.5582
9*	0.9926	0.5981
365	0.9928	0.7331
496	0.9929	0.7283
196a	0.9931	0.8389
199b-5p	0.9932	0.8278
128	0.9936	0.7831
7-1*	0.9936	0.8033
27b	0.9940	0.5410
30c-2*	0.9941	0.8232
154	0.9942	0.8464
335*	0.9943	0.8297
411-3p	0.9949	0.7627
615-5p	0.9949	0.8524
181c	0.9954	0.8416
302c	0.9957	0.7313
miR-192	0.9962	0.7612
19a	0.9962	0.8113
122	0.9962	0.9328
99b*	0.9965	0.8130
222	0.9967	0.9180
532-5p	0.9970	0.7646

191	0.9973	0.9101
26a	0.9978	0.8145
142-3p	0.9980	0.8954
147b	0.9982	0.9504
759	0.9985	0.9368
370	0.9990	0.9713
miR-203	0.9991	0.9662
410	0.9994	0.9789
30e	0.9997	0.9848
423-3p	0.9998	0.9907
23b	1.0002	0.9774
195	1.0008	0.9449
214*	1.0009	0.9570
26b	1.0014	0.9581
22	1.0014	0.9011
29b	1.0022	0.7976
539	1.0023	0.8486
miR-10a	1.0024	0.9136
185	1.0025	0.9727
99b	1.0026	0.8401
126	1.0031	0.7665

194	1.0032	0.9329
495	1.0035	0.7605
363	1.0039	0.8851
214	1.0048	0.9104
27b*	1.0051	0.8179
miR-18a	1.0057	0.7484
379	1.0058	0.8609
193a-3p	1.0062	0.7570
99a	1.0063	0.6499
487a	1.0066	0.8082
409-3p	1.0068	0.6647
378	1.0072	0.5615
433	1.0074	0.6977
219-5p	1.0076	0.7270
450a	1.0079	0.7258
323b-5p	1.0084	0.6692
miR-367	1.0088	0.5249
451	1.0091	0.6485
205	1.0092	0.3560
101	1.0094	0.8416
376a	1.0100	0.8133
486-5p	1.0101	0.7486

let-7d-3p	1.0103	0.6978
532-3p	1.0103	0.2611
20a	1.0107	0.2441
302d	1.0109	0.4091
148a	1.0113	0.6905
302a	1.0116	0.6585
151-5p	1.0123	0.6524
124	1.0124	0.4527
181a*	1.0132	0.5294
let-7b	1.0141	0.7430
17	1.0143	0.5803
let7i-3p	1.0146	0.7406
653	1.0158	0.4709
200b*	1.0159	0.6637
340	1.0179	0.5953
216a	1.0194	0.3011
877	1.0195	0.3540
miR-28-5p	1.0195	0.3572
150	1.0196	0.1798
382	1.0202	0.3414
106b*	1.0205	0.4636

miR-134	1.0206	0.1047
557	1.0208	0.2075
335	1.0214	0.5684
125a-5p	1.0214	0.4840
let-7d	1.0218	0.2582
421	1.0218	0.5686
208b	1.0226	0.5531
369-3p	1.0234	0.0512
let-7b-3p	1.0243	0.1523
708	1.0246	0.3646
875-5p	1.0247	0.2305
148a*	1.0255	0.1098
let-7e	1.0257	0.4493
15b*	1.0257	0.3946
218	1.0268	0.4222
127-5p	1.0279	0.2546
663	1.0282	0.5465
30c	1.0295	0.1836
186	1.0315	0.0744
378*	1.0324	0.0350
130a	1.0331	0.3390
miR-190b	1.0336	0.1404

431-3p	1.0338	0.1775
30d	1.0348	0.1685
299-5p	1.0361	0.0149
26b*	1.0362	0.1088
671-5p	1.0390	0.2123
107	1.0393	0.0464
125b-1-3p	1.0396	0.0261
449a	1.0410	0.0080
34a	1.0410	0.2661
30b	1.0436	0.0213
130b	1.0438	0.2378
320a	1.0448	0.2536
20b	1.0456	0.1832
654-3p	1.0462	0.0345
140-3p	1.0498	0.2255
409-5p	1.0522	0.1056
711	1.0550	0.0640
146b-5p	1.0553	0.1623
374b	1.0563	0.0088
19b	1.0574	0.3611
338-5p	1.0576	0.0105

126*	1.0606	0.0714
92b	1.0660	0.0071
181b	1.0682	0.0347
miR-125a-3p	1.0713	0.0114
378b	1.0720	0.0160
590-3p	1.0736	0.0524
218-2*	1.0745	0.3343
143	1.0844	0.0006
30e*	1.0850	0.0018
145	1.0874	0.0764
199b-3p	1.0886	0.1952
15a	1.1544	0.0674

REFERENCES

[1] Go, A. S., D. Mozaffarian, V. L. Roger, and et al. Heart disease and stroke statistics-2013 update: a report from the American Heart Association. Circulation. 2013; 127(1): e6-e245.

[2] Thygesen, K., J. S. Alpert, H. D. White, A. S. Jaffe, and et al. Universal definition of myocardial infarction. Circulation, 2007; 116(22): 2634-2653.

[3] Hearse, D. J. Myocardial ischaemia: can we agree on a definition for the 21st century? Cardiovasc Res. 1994; 28(12): 1737-1744: discussion 1745-1736.

[4] Van Wylen, D. G., R. Baxamusa, J. Berge, K. Bothun, J. E. Elvecrog, R. Eriksmoen, E. Julsrud, J. M. Fay, B. Kelly, A. Menter and et al. Definition of ischaemia. Cardiovasc Res. 1995; 29(5): 727.

[5] Verdouw, P. D., M. A. van den Doel, S. de Zeeuw and D. J. Duncker. Animal models in the study of myocardial ischaemia and ischaemic syndromes. Cardiovasc Res. 1998; 39(1): 121-135.

[6] Asano, G., E. Takashi, T. Ishiwata, M. Onda, M. Yokoyama, Z. Naito, M. Ashraf and Y. Sugisaki. Pathogenesis and protection of ischemia and reperfusion injury in myocardium. J Nippon Med Sch. 2003; 70(5): 384-392.

[7] Michiels, C. Physiological and pathological responses to hypoxia. Am J Pathol. 2004; 164(6): 1875-1882.

[8] Chiong, M., Z. V. Wang, Z. Pedrozo, D. J. Cao, R. Troncoso, M. Ibacache, A. Criollo, A. Nemchenko, J. A. Hill and S. Lavandero. Cardiomyocyte death: mechanisms and translational implications. Cell Death Dis. 2011; 2: e244.
Mill, J. G., I. Stefanon, L. dos Santos and M. P. Baldo. Remodeling in the ischemic heart: the stepwise progression for heart failure. Braz J Med Biol Res. 2011; 44(9): 890--898.

[9] Harken, A. H., M. B. Simson, J. Haselgrove, L. Wetstein, W. R. Harden, 3rd and C. H. Barlow. Early ischemia after complete coronary ligation in the rabbit, dog, pig, and monkey. Am J Physiol. 1981; 241(2): H202-210.

[10] Himori, N. and A. Matsuura. A simple technique for occlusion and reperfusion of coronary artery in conscious rats. Am J Physiol. 1989; 256(6 Pt 2): H1719-1725.

[11] Cohen, M. V., G. S. Liu and J. M. Downey. Preconditioning causes improved wall motion as well as smaller infarcts after transient coronary occlusion in rabbits. Circulation. 1991; 84(1): 341-349.

[12] Tarnavski, O., J. R. McMullen, M. Schinke, Q. Nie, S. Kong and S. Izumo. Mouse cardiac surgery: comprehensive techniques for the generation of mouse models of human diseases and their application for genomic studies. Physiol Genomics. 2004; 16(3): 349-360.

[13] Frangogiannis, N. G., C. W. Smith and M. L. Entman. The inflammatory response in myocardial infarction. Cardiovasc Res. 2002; 53(1): 31-47.

[14] Nian, M., P. Lee, N. Khaper and P. Liu (2004). "Inflammatory cytokines and postmyocardial infarction remodeling." Circ Res 94(12): 1543-1553.

[15] Dobaczewski, M. and N. G. Frangogiannis. Chemokines and cardiac fibrosis. Front Biosci (Schol Ed). 2009; 1: 391-405.

[16] Frangogiannis, N. G. Regulation of the inflammatory response in cardiac repair. Circ Res. 2012; 110(1): 159-173.

[17] Rosenthal, K. S., S. Drakovac and S. Stone. Disease Outcomes Are Influenced by the Yang (M1) or Yin (M2) of Macrophage Function. Infectious Diseases in Clinical Practice. 2012; 20(4): 272-276.

[18] Dobaczewski, M., W. Chen and N. G. Frangogiannis. Transforming growth factor (TGF)-beta signaling in cardiac remodeling. J Mol Cell Cardiol. 2011; 51(4): 600-606.

[19] Sun, Y. and K. T. Weber. Angiotensin-converting enzyme and wound healing in diverse tissues of the rat. Journal of Laboratory & Clinical Medicine. 1996; 127(1): 94-101.

[20] Porter, K. E. and N. A. Turner. Cardiac fibroblasts: at the heart of myocardial remodeling. Pharmacol Ther. 2009; 123(2): 255-278.

[21] Pfeffer, J. M., M. A. Pfeffer and E. Braunwald. Influence of chronic captopril therapy on the infarcted left ventricle of the rat. Circ Res. 1985; 57(1): 84-95.

[22] Opie, L. H., P. J. Commerford, B. J. Gersh and M. A. Pfeffer. Controversies in ventricular remodelling. Lancet. 2006; 367(9507): 356-367.

[23] Weisman, H. F., D. E. Bush, J. A. Mannisi, M. L. Weisfeldt and B. Healy. Cellular mechanisms of myocardial infarct expansion. Circulation. 1998; 78(1): 186-201.

[24] Zamilpa, R. and M. L. Lindsey. Extracellular matrix turnover and signaling during cardiac remodeling following MI: causes and consequences. J Mol Cell Cardiol. 2010; 48(3): 558-563.

[25] Anversa, P., C. Beghi, Y. Kikkawa and G. Olivetti. Myocardial response to infarction in the rat. Morphometric measurement of infarct size and myocyte cellular hypertrophy. Am J Pathol. 1985; 118(3): 484-492.

[26] Pfeffer, M. A. and E. Braunwald. Ventricular remodeling after myocardial infarction. Experimental observations and clinical implications. Circulation. 1990; 81(4): 1161-1172.

[27] Bayat, H., J. S. Swaney, A. N. Ander, N. Dalton, B. P. Kennedy, H. K. Hammond and D. M. Roth. Progressive heart failure after myocardial infarction in mice. Basic Res Cardiol. 2002; 97(3): 206-213.

[28] John, B. T., B. K. Tamarappoo, J. L. Titus, W. D. Edwards, W. K. Shen and S. S. Chugh. Global remodeling of the ventricular interstitium in idiopathic myocardial fibrosis and sudden cardiac death. Heart Rhythm. 2004; 1(2): 141-149.

[29] Frey, N. and E. N. Olson. Cardiac hypertrophy: the good, the bad, and the ugly. Annu Rev Physiol. 2003; 65: 45-79.

[30] Gao, X. M., A. M. Dart, E. Dewar, G. Jennings and X. J. Du. Serial echocardiographic assessment of left ventricular dimensions and function after myocardial infarction in mice. Cardiovasc Res. 2000; 45(2): 330-338.

[31] Swynghedauw, B. Molecular mechanisms of myocardial remodeling. Physiol Rev. 1999; 79(1): 215-262.

[32] Looi, Y. H., D. J. Grieve, A. Siva, S. J. Walker, N. Anilkumar, A. C. Cave, M. Marber, M. J. Monaghan and A. M. Shah. Involvement of Nox2 NADPH oxidase in adverse cardiac remodeling after myocardial infarction. Hypertension. 2008; 51(2): 319-325.

[33] Cave, A. Selective targeting of NADPH oxidase for cardiovascular protection. Curr Opin Pharmacol. 2009; 9(2): 208-213.

[34] Cave, A. C., A. C. Brewer, A. Narayanapanicker, R. Ray, D. J. Grieve, S. Walker and A. M. Shah. NADPH oxidases in cardiovascular health and disease. Antioxid Redox Signal. 2006; 8(5-6): 691-728.

[35] Bendall, J. K., A. C. Cave, C. Heymes, N. Gall and A. M. Shah. Pivotal role of a gp91(phox)-containing NADPH oxidase in angiotensin II-induced cardiac hypertrophy in mice. Circulation. 2002; 105(3): 293-296.

[36] Krijnen, P. A., C. Meischl, C. E. Hack, C. J. Meijer, C. A. Visser, D. Roos and H. W. Niessen. Increased Nox2 expression in human cardiomyocytes after acute myocardial infarction. J Clin Pathol. 2003; 56(3): 194-199.

[37] Heymes, C., J. K. Bendall, P. Ratajczak, A. C. Cave, J. L. Samuel, G. Hasenfuss and A. M. Shah (2003). Increased myocardial NADPH oxidase activity in human heart failure. J Am Coll Cardiol. 2003; 41(12): 2164-2171.

[38] Grieve, D. J., J. A. Byrne, A. Siva, J. Layland, S. Johar, A. C. Cave and A. M. Shah (2006). Involvement of the nicotinamide adenosine dinucleotide phosphate oxidase isoform Nox2 in cardiac contractile dysfunction occurring in response to pressure overload. J Am Coll Cardiol. 2006; 47(4): 817-826.

[39] Somasuntharam, I., A. V. Boopathy, R. S. Khan, M. D. Martinez, M. E. Brown, N. Murthy and M. E. Davis (2013). Delivery of Nox2-NADPH oxidase siRNA with polyketal nanoparticles for improving cardiac function following myocardial infarction. Biomaterials. 2013; 34(31): 7790-7798.

[40] Lee R, Feinbaum R, Ambros V. The C. elegans heterochronic gene lin-4 encodes small RNAs with antisense complementarity to lin-14. Cell. 1993; 75: 843-897.

[41] Moss E, Lee R, Ambros V. The cold shock domain protein LIN-28 controls developmental timing in C. elegans and is regulated by the lin-4 RNA. Cell. 1997; 88: 637- 683.

[42] Reinhart B, Slack F, Basson M, Pasquinelli A, Bettinger J, Rougvie A et al. The 21-

nucleotide let-7 RNA regulates developmental timing in Caenorhabditis elegans. Nature. 2000; 403: 901-907.

[43] Wightman B, Ha I, Ruvkun G. Posttranscriptional regulation of the heterochronic gene lin-14 by lin-4 mediates temporal pattern formation in C. elegans. Cell. 1993; 75: 855-917.

[44] Pasquinelli A, Reinhart B, Slack F, Martindale M, Kuroda M, Maller B et al. Conservation of the sequence and temporal expression of let-7 heterochronic regulatory RNA. Nature. 2000; 408: 86-95.

[45] Lagos-Quintana M, Rauhut R, Lendeckel W, Tuschl T. Identification of novel genes coding for small expressed RNAs. Science (New York, NY). 2001; 294: 853-861

[46] Lau N, Lim L, Weinstein E, Bartel D. An abundant class of tiny RNAs with probable regulatory roles in Caenorhabditis elegans. Science (New York, NY). 2001; 294: 858-920.

[47] Lee R, Ambros V. An extensive class of small RNAs in Caenorhabditis elegans. Science (New York, NY). 2001; 294: 862-866.

[48] Bartel D. MicroRNAs: target recognition and regulatory functions. Cell. 2009 136: 215-248.

[49] He L, Hannon G. MicroRNAs: small RNAs with a big role in gene regulation. Nature reviews Genetics. 2004; 5: 522-553.

[50] Chekulaeva M, Filipowicz W. Mechanisms of miRNA-mediated post- transcriptional regulation in animal cells. Current opinion in cell biology. 2009; 21: 452-512.

[51] Thum T, Gross C, Fiedler J, et al. MicroRNA-21 contributes to myocardial disease by stimulating MAP kinase signalling in fibroblasts. Nature. 2008; 456:980–984.

[52] Van Rooij E, Sutherland LB, Thatcher JE, DiMaio JM, Naseem RH, Marshall WS, Hill JA, Olson EN. Dysregulation of microRNAs after myocardial infarction reveals a role of miR-29 in cardiac fibrosis. Proc Natl Acad Sci USA. 2008; 105:13027–13032.

[53] Carè A, Catalucci D, Felicetti F, et al. MicroRNA-133 controls cardiac hypertrophy. Nat Med. 2007; 13:613–618.

[54] Bonauer A, Carmona G, Iwasaki M, et al. MicroRNA-92a controls angiogenesis and functional recovery of ischemic tissues in mice. Science. 2009; 324:1710–1713.

[55] Fiedler J, Jazbutyte V, Kirchmaier BC, et al. MicroRNA-24 regulates vascularity after myocardial infarction. Circulation. 2011; 124:720–730.

[56] Widera C, Gupta SK, Lorenzen JM, Bang C, Bauersachs J, Bethmann K, Kempf T, Wollert KC, Thum T. Diagnostic and prognostic impact of six circulating microRNAs in acute coronary syndrome. J Mol Cell Cardiol. 2011; 51:872–875.

[57] Zampetaki A, Willeit P, Tilling L, Drozdov I, Prokopi M, and et al. Prospective study on circulating MicroRNAs and risk of myocardial infarction. J Am Coll Cardiol. 2012;

60:290–299.

[58] Devaux Y, Vausort M, Goretti E, Nazarov PV, Azuaje F, Gilson G, Corsten MF, Schroen B, Lair ML, Heymans S, Wagner DR. Use of circulating microRNAs to diagnose acute myocardial infarction. Clin Chem. 2012; 58:559–567.

[59] Thomson, D. W., C. P. Bracken and G. J. Goodall. Experimental strategies for microRNA target identification. Nucleic Acids Res. 2011; 39(16): 6845-6853.

[60] 61. Hafner, M., M. Landthaler, L. Burger, M. Khorshid, J. Hausser, P. Berninger, A. Rothballer, M. Ascano, Jr., A. C. Jungkamp, M. Munschauer, A. Ulrich, G. S. Wardle, S. Dewell, M. Zavolan and T. Tuschl. Transcriptome-wide identification of RNA-binding protein and microRNA target sites by PAR-CLIP. Cell. 2010; 141(1): 129-141.

[61] Orom, U. A. and A. H. Lund. Experimental identification of microRNA targets. Gene. 2010; 451(1-2): 1-5.

[62] Yin, S., Y. Fan, H. Zhang, Z. Zhao, Y. Hao, J. Li, C. Sun, J. Yang, Z. Yang, X. Yang, J. Lu and J. J. Xi. Differential TGFbeta pathway targeting by miR-122 in humans and mice affects liver cancer metastasis. Nat Commun. 2016; 7: 11012.

[63] Yang YY, Chung TS, Ng NP. Morphology, drug distribution, and in vitro release profiles of biodegradable polymeric microspheres containing protein fabricated by double-emulsion solvent extraction/evaporation method. Biomaterials. 2001; 22(3):231–41.

[64] Wilson DS, Dalmasso G, Wang L, Sitaraman SV, Merlin, DMurthy N. Orally delivered thioketal nanoparticles loaded with TNF-alpha-siRNA target inflammation and inhibit gene expression in the intestines. Nat Mater. 2010; 9(11):923–8.

[65] Sy JC, Seshadri G, Yang SC, Brown M, Oh T, Dikalov S, et al. Sustained release of a p38 inhibitor from non-inflammatory microspheres inhibits cardiac dysfunction. Nat Mater. 2008; 7(11):863–8.

[66] Yang SC, Bhide M, Crispe IN, Pierce RH, Murthy N. Polyketal copolymers: a new acid-sensitive delivery vehicle for treating acute inflammatory diseases. Bioconjug Chem. 2008; 19(6):1164–9.

[67] Seshadri G, Sy JC, Brown M, Dikalov S, Yang SC, Murthy N, et al. The delivery of superoxide dismutase encapsulated in polyketal microparticles to rat myocardium and protection from myocardial ischemia-reperfusion injury. Biomaterials. 2010; 31(6):1372–9.

[68] Lee S, Yang SC, Kao CY, Pierce RH, Murthy N. Solid polymeric microparticles enhance the delivery of siRNA to macrophages in vivo. Nucleic Acids Res. 2009; 37(22):e145.

[69] Ferdinandy, P. and R. Schulz. Nitric oxide, superoxide, and peroxynitrite in myocardial ischaemia-reperfusion injury and preconditioning. Br J Pharmacol. 2003; 138(4): 532-543.

[70] Looi, Y. H., D. J. Grieve, A. Siva, S. J. Walker, N. Anilkumar, A. C. Cave, M. Marber, M. J. Monaghan and A. M. Shah. Involvement of Nox2 NADPH oxidase in adverse cardiac

remodeling after myocardial infarction. Hypertension. 2008; 51(2): 319-325.

[71] Cave, A. Selective targeting of NADPH oxidase for cardiovascular protection. Curr Opin Pharmacol. 2009; 9(2): 208-213.

[72] Bendall, J. K., A. C. Cave, C. Heymes, N. Gall and A. M. Shah. Pivotal role of a gp91(phox)-containing NADPH oxidase in angiotensin II-induced cardiac hypertrophy in mice. Circulation. 2002; 105(3): 293-296.

[73] Krijnen, P. A., C. Meischl, C. E. Hack, C. J. Meijer, C. A. Visser, D. Roos and H. W. Niessen. Increased Nox2 expression in human cardiomyocytes after acute myocardial infarction. J Clin Pathol. 2003; 56(3): 194-199.

[74] Heymes, C., J. K. Bendall, P. Ratajczak, A. C. Cave, J. L. Samuel, G. Hasenfuss and A. M. Shah (2003). Increased myocardial NADPH oxidase activity in human heart failure. J Am Coll Cardiol. 2003; 41(12): 2164-2171.

[75] Liu, Z., D. Yang, P. Xie, G. Ren, G. Sun, X. Zeng and X. Sun. MiR-106b and MiR-15b modulate apoptosis and angiogenesis in myocardial infarction. Cell Physiol Biochem. 2012; 29(5-6): 851-862.

[76] Chuang, T. D., X. Luo, H. Panda and N. Chegini. miR-93/106b and their host gene, MCM7, are differentially expressed in leiomyomas and functionally target F3 and IL-8. Mol Endocrinol. 2012; 26(6): 1028-1042.

[77] Liu, X., Z. Zhan, L. Xu, F. Ma, D. Li, Z. Guo, N. Li and X. Cao. MicroRNA-148/152 impair innate response and antigen presentation of TLR-triggered dendritic cells by targeting CaMKIIalpha. J Immunol. 2010; 185(12): 7244-7251.

[78] Yang, Q., J. Cui, P. Wang, X. Du, W. Wang, T. Zhang and Y. Chen. Changes in interconnected pathways implicating microRNAs are associated with the activity of apocynin in attenuating myocardial fibrogenesis. Eur J Pharmacol. 2016; 784: 22-32.

[79] Xiao, J., X. Zhu, B. He, Y. Zhang, B. Kang, Z. Wang and X. Ni. MiR-204 regulates cardiomyocyte autophagy induced by ischemia-reperfusion through LC3-II. J Biomed Sci. 2011; 18: 35.

[80] Carthew, R. W. and E. J. Sontheimer. Origins and Mechanisms of miRNAs and siRNAs. Cell. 2009; 136(4): 642-655

[81] Judge, A. D., V. Sood, J. R. Shaw, D. Fang, K. McClintock and I. MacLachlan. Sequence-dependent stimulation of the mammalian innate immune response by synthetic siRNA. Nat Biotechnol. 2005; 23(4): 457-462.

[82] Johnson, C. D., A. Esquela-Kerscher, G. Stefani, M. Byrom, K. Kelnar, D. Ovcharenko, M. Wilson, X. Wang, J. Shelton, J. Shingara, L. Chin, D. Brown and F. J. Slack. The let-7 microRNA represses cell proliferation pathways in human cells. Cancer Res. 2007; 67(16): 7713-7722.

[83] Zhang, H., Y. Hao, J. Yang, Y. Zhou, J. Li, S. Yin, C. Sun, M. Ma, Y. Huang and J. J. Xi. Genome-wide functional screening of miR-23b as a pleiotropic modulator suppressing

cancer metastasis. Nat Commun. 2011; 2: 554.

[84] Gray, W. D., P. Che, M. Brown, X. Ning, N. Murthy and M. E. Davis. N-acetylglucosamine conjugated to nanoparticles enhances myocyte uptake and improves delivery of a small molecule p38 inhibitor for post-infarct healing. J Cardiovasc Transl Res. 2011; 4(5): 631-643.

[85] Danilenko, V. V. On the history of the discovery of nanodiamond synthesis. Phys. Solid State. 2004; 46, 595–599.

[86] Greiner, N. R., Phillips, D. S., Johnson, J. D. & Volk, F. Diamonds in detonation soot. Nature. 1988; 333, 440–442.

[87] Ozawa, M. et al. Preparation and behavior of brownish, clear nanodiamond colloids. Adv. Mater. 2007; 19, 1201–1206.

[88] Chang, Y. R. et al. Mass production and dynamic imaging of fluorescent nanodiamonds. Nature Nanotech. 2008; 3, 284–288.

[89] Schrand, A. M. et al. in Safety of Nanoparticles. From Manufacturing to Medical Applications. Nanostructure Science and Technology (ed. Webster, T. J.). 2009; 159–187.

[90] Schrand, A. M., Hens, S. A. C. & Shenderova, O. A. Nanodiamond particles: Properties and perspectives for bioapplications. Crit. Rev. Solid State Mater. Sci. 2009; 34, 18–74.

[91] Yang, G. W., Wang, J. B. & Liu, Q. X. Preparation of nano-crystalline diamonds using pulsed laser induced reactive quenching. J. Phys. Condens. Mat. 1998; 10, 7923–7927.

[92] Frenklach, M. et al. Induced nucleation of diamond powder. Appl. Phys. Lett. 1991; 59, 546–548.

[93] Daulton, T. L., Kirk, M. A., Lewis, R. S. & Rehn, L. E. Production of nanodiamonds by high-energy ion irradiation of graphite at room temperature. Nucl. Instrum. Meth. B. 2001; 175, 12–20.

[94] Galimov, É. et al. Experimental corroboration of the synthesis of diamond in the cavitation process. Dokl. Phys. 2004; 49, 150–153.

[95] Hens, S. C. et al. Nanodiamond bioconjugate probes and their collection by electrophoresis. Diamond Relat. Mater. 2008; 17, 1858–1866.

[96] Huang, L. C. L. & Chang, H. C. Adsorption and immobilization of cytochrome C on nanodiamonds. Langmuir. 2004; 20, 5879–5884.

[97] 98. Faklaris, O. et al. Photoluminescent diamond nanoparticles for cell labeling: Study of the uptake mechanism in mammalian cells. ACS Nano. 2009; 3, 3955–3962.

[98] Yuan, Y. et al. Pulmonary toxicity and translocation of nanodiamonds in mice. Diamond Relat. Mater. 2010; 19, 291–299.

[99] Mohan, N., Chen, C. S., Hsieh, H. H., Wu, Y. C. & Chang, H. C. In vivo imaging and toxicity assessments of fluorescent nanodiamonds in Caenorhabditis elegans. Nano Lett. 2010; 10, 3692–3699.

[100] Chow, E. K. et al. Nanodiamond therapeutic delivery agents mediate enhanced chemoresistant tumor treatment. Sci. Transl. Med. 2011; 3, 73ra21.

[101] Zhang, X. Q. et al. Polymer-functionalized nanodiamond platforms as vehicles for gene delivery. ACS Nano. 2009; 3, 2609–2616.

[102] Chen, M. et al. Nanodiamond vectors functionalized with polyethylenimine for siRNA delivery. J. Phys. Chem. Lett. 2010; 1, 3167–3171.

[103] Chow, E. K. et al. Nanodiamond therapeutic delivery agents mediate enhanced chemoresistant tumor treatment. Sci. Transl. Med. 2011; 3, 73ra21.

[104] Thalhammer, A., Edgington, R. J., Cingolani, L. A., Schoepfer, R. & Jackman, R. B. The use of nanodiamond monolayer coatings to promote the formation of functional neuronal networks. Biomaterials. 2010; 31, 2097–2104.

[105] Wang, H.; Niu, Y. Y.; Si, W.; Li, J. Y.; Yan, Y.Reference Data of Clinical Chemistry, Haematology and Blood Coagulation Parameters in Juvenile Cynomolgus Monkeys (Macaca Fascicularis) Vet. Med. 2012,; 57, 233– 238

[106] Peppas, Nicholas A.; Hilt, J. Zach; Khademhosseini, Ali; Langer, Robert. Hydrogels in biology and medicine: from molecular principles to bionanotechnology. Advanced Materials (Weinheim, Germany). 2006, 18 (11), 1345-1360

[107] Peer, Dan; Karp, Jeffrey M.; Hong, Seungpyo; Farokhzad, Omid C.; Margalit, Rimona; Langer, Robert. Nanocarriers as an emerging platform for cancer therapy. Nature Nanotechnology. 2007; 2 (12), 751-760

[108] Faklaris, Orestis; Joshi, Vandana; Irinopoulou, Theano; Tauc, Patrick; Sennour, Mohamed; Girard, Hugues; Gesset, Celine; Arnault, Jean-Charles; Thorel, Alain; Boudou, Jean-Paul; Curmi, Patrick A.; Treussart, Francois. Photoluminescent Diamond Nanoparticles for Cell Labeling: Study of the Uptake Mechanism in Mammalian Cell. ACS Nano. 2009; 3 (12), 3955-3962

[109] Wu, Tsai-Jung; Tzeng, Yan-Kai; Chang, Wei-Wei; Cheng, Chi-An; Kuo, Yung; Chien, Chin-Hsiang; Chang, Huan-Cheng; Yu, John. Tracking the engraftment and regenerative capabilities of transplanted lung stem cells using fluorescent nanodiamonds. Nature Nanotechnology. 2013; 8 (9), 682-689

[110] Moore, Laura; Chow, Edward Kai-Hua; Osawa, Eiji; Bishop, J. Michael; Ho, Dean. Diamond-Lipid Hybrids Enhance Chemotherapeutic Tolerance and Mediate Tumor Regression. Advanced Materials (Weinheim, Germany). 2013; 25 (26), 3532-3541

[111] Manus, Lisa M.; Mastarone, Daniel J.; Waters, Emily A.; Zhang, Xue-Qing; Schultz-Sikma, Elise A.; MacRenaris, Keith W.; Ho, Dean; Meade, Thomas J. Gd(III)-Nanodiamond Conjugates for MRI Contrast Enhancement. Nano Letters. 2010; 10 (2), 484-489

[112] Wang, Xin; Low, Xinyi Casuarine; Hou, Weixin; Abdullah, Lissa Nurrul; Toh, Tan Boon; Mohd Abdul Rashid, Masturah; Ho, Dean; Chow, Edward Kai-Hua. Epirubicin-

Adsorbed Nanodiamonds Kill Chemoresistant Hepatic Cancer Stem Cells. ACS Nano. 2014; 8 (12), 12151-12166

[113] Yuan, Y.; Chen, Y.; Liu, J.-H.; Wang, H.; Liu, Y.Biodistribution and Fate of Nanodiamonds Diamond Relat. Mater. 2009; 18, 95-100.